Article
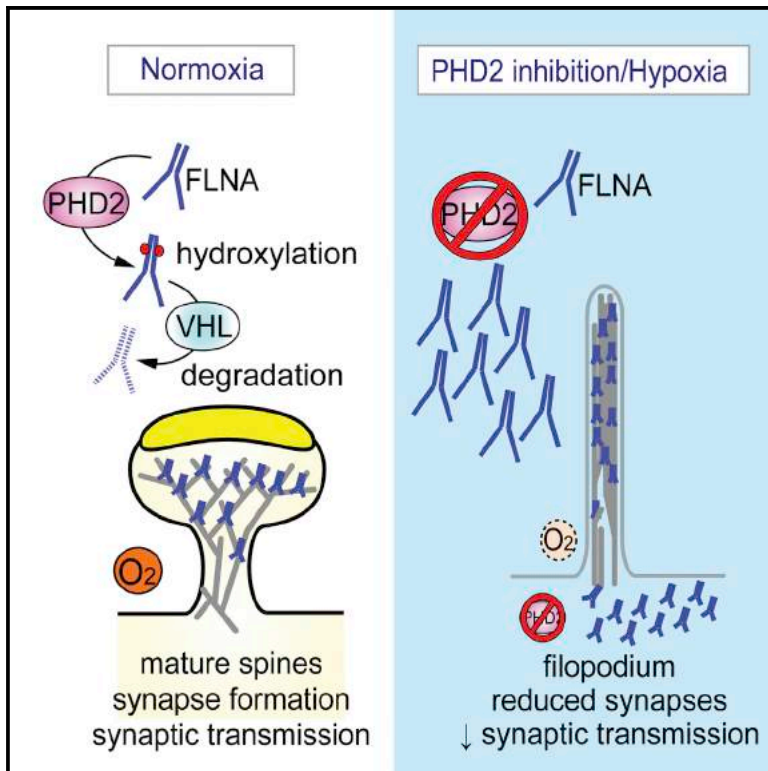
The Oxygen Sensor PHD2 Controls Dendritic Spines and Synapses via Modification of Filamin A

Graphical Abstract

Authors

Inmaculada Segura, Christian Lange, Ellen Knevels, ..., Carmen Ruiz de Almodovar, Mieke Dewerchin, Peter Carmeliet

Correspondence

peter.carmeliet@vib-kuleuven.be

In Brief

Neuronal function is highly sensitive to oxygen levels. Segura et al. show that inhibition of the oxygen sensor PHD2 induces dendritic spine regression in hippocampal neurons, thereby reducing synaptic density and network-wide neuronal activity. We identify the actin cross-linker filamin A as a target of PHD2 mediating these effects.

Highlights

- The oxygen sensor PHD2 is present in dendritic spines

- PHD2 inhibition by hypoxia reduces spine maturation, synaptic density, and activity

- Through hydroxylation, PHD2 targets filamin A for proteasomal degradation

- Filamin A stabilization promotes dendritic spine remodeling

CellPress

The Oxygen Sensor PHD2 Controls Dendritic Spines and Synapses via Modification of Filamin A

Inmaculada Segura,[1,2,10] Christian Lange,[1,2,10] Ellen Knevels,[1,2] Anastasiya Moskalyuk,[3] Rocco Pulizzi,[3] Guy Eelen,[1,2] Thibault Chaze,[4] Cicerone Tudor,[5] Cyril Boulegue,[4] Matthew Holt,[5] Dirk Daelemans,[6] Mariette Matondo,[4] Bart Ghesquière,[7] Michele Giugliano,[3,8,9] Carmen Ruiz de Almodovar,[1,2,11] Mieke Dewerchin,[1,2] and Peter Carmeliet[1,2,*]
[1]Laboratory of Angiogenesis and Vascular Metabolism, Department of Oncology, KU Leuven, 3000 Leuven, Belgium
[2]Laboratory of Angiogenesis and Vascular Metabolism, Vesalius Research Center, VIB, 3000 Leuven, Belgium
[3]Laboratory of Theoretical Neurobiology and Neuroengineering, University of Antwerp, 2610 Wilrijk, Belgium
[4]Proteomics Platform, Institute Pasteur, 75015 Paris, France
[5]Laboratory of Glia Biology, VIB, 3000 Leuven, Belgium
[6]Laboratory of Virology and Chemotherapy, Rega Institute, KU Leuven, 3000 Leuven, Belgium
[7]Metabolomics Core Facility, Vesalius Research Center, VIB, 3000 Leuven, Belgium
[8]Neuro-Electronics Research Flanders, 3001 Leuven, Belgium
[9]Brain Mind Institute, Swiss Federal Institute of Technology of Lausanne, 1015 Lausanne, Switzerland
[10]Co-first author
[11]Present address: Biochemistry Center, Heidelberg University, 69120 Heidelberg, Germany
*Correspondence: peter.carmeliet@vib-kuleuven.be
http://dx.doi.org/10.1016/j.celrep.2016.02.047

SUMMARY

Neuronal function is highly sensitive to changes in oxygen levels, but how hypoxia affects dendritic spine formation and synaptogenesis is unknown. Here we report that hypoxia, chemical inhibition of the oxygen-sensing prolyl hydroxylase domain proteins (PHDs), and silencing of *Phd2* induce immature filopodium-like dendritic protrusions, promote spine regression, reduce synaptic density, and decrease the frequency of spontaneous action potentials independently of HIF signaling. We identified the actin cross-linker filamin A (FLNA) as a target of PHD2 mediating these effects. In normoxia, PHD2 hydroxylates the proline residues P2309 and P2316 in FLNA, leading to von Hippel-Lindau (VHL)-mediated ubiquitination and proteasomal degradation. In hypoxia, PHD2 inactivation rapidly upregulates FLNA protein levels because of blockage of its proteasomal degradation. FLNA upregulation induces more immature spines, whereas *Flna* silencing rescues the immature spine phenotype induced by PHD2 inhibition.

INTRODUCTION

Synaptic transmission is the main energy-consuming process in the brain and requires large amounts of ATP. Because neurons generate energy primarily oxidatively, they require oxygen. Therefore, when oxygen becomes limiting, there is a risk that the ATP pool becomes exhausted. We hypothesized that neurons possess adaptive mechanisms to prevent such an energy crisis during hypoxia and speculated that hypoxia might remodel dendritic spines to reduce the energy-consuming process of synaptic transmission.

The oxygen sensors prolyl hydroxylase domain-containing proteins (PHD1-3) use oxygen to hydroxylate prolines in target proteins, such as hypoxia-inducible transcription factor α (HIFα) (Epstein et al., 2001). Hydroxylated HIFα is ubiquitinated by the E3 ubiquitin ligase von Hippel-Lindau (VHL), triggering proteasomal degradation (Ivan et al., 2001; Jaakkola et al., 2001). In hypoxia, PHDs are inactive, and stabilized HIFα upregulates the transcription of target genes (Epstein et al., 2001). PHDs also have HIF- and hydroxylation-independent functions and targets (Wong et al., 2013).

Dendritic spines are actin-rich protrusions emerging from dendrites and receiving synaptic input. They are implicated in synaptic plasticity, learning, and memory (Hotulainen and Hoogenraad, 2010). Spines sprout as filopodia that search for synaptic contact and develop into mature spines containing the postsynaptic density receiving synaptic input (Ethell and Pasquale, 2005; Hotulainen and Hoogenraad, 2010). Among actin cross-linkers, filamin A (FLNA) promotes the formation of orthogonal networks or parallel actin bundles, depending on the filamin/F-actin ratio (van der Flier and Sonnenberg, 2001). FLNA regulates dendritic morphogenesis (Zhang et al., 2014), the axonal growth cone (Zheng et al., 2011), and neuronal migration (Sarkisian et al., 2006), but it is unknown whether FLNA regulates spine morphology. Notably, under- and overexpression of FLNA impair neuronal migration via distinct mechanisms (Sarkisian et al., 2006; Zhang et al., 2012, 2013), indicating that neurons require precise regulation of FLNA levels.

Anecdotal observations suggest that PHDs regulate actin rearrangements via an undefined mechanism. PHD2-haplodeficient endothelial cells have impaired migration and actin cytoskeleton reorganization (Mazzone et al., 2009), whereas PHD2-deficient HeLa cells show altered cell migration via an HIF-independent mechanism (Vogel et al., 2010). These findings
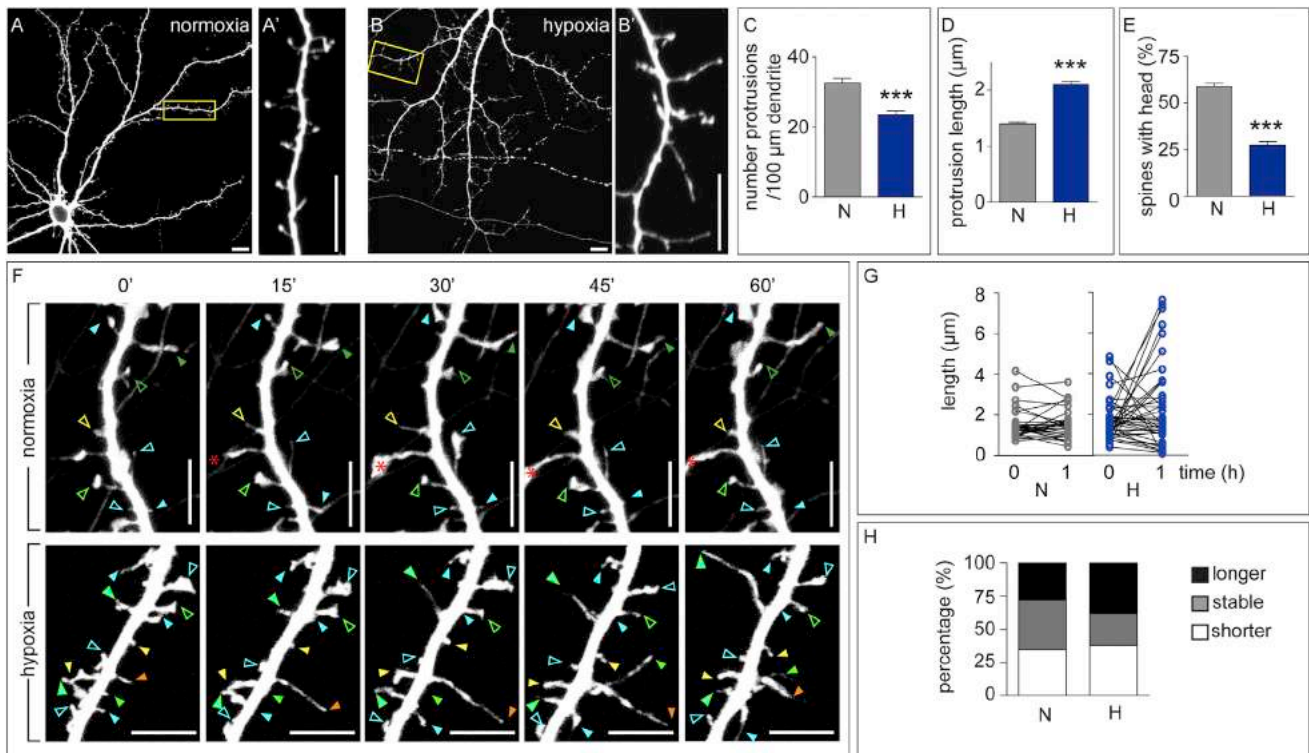
Figure 1. The Effect of Hypoxia on Dendritic Spines

(A–E) YFP-transfected MHNs were incubated for 16 hr in normoxia (A) or hypoxia (B) and analyzed for protrusion density (C), protrusion length (D), and percentage of spines with a head (E) (n = 3 experiments, 30 neurons, >800 protrusions). (A′) and (B′) show higher magnifications of the boxes in (A) and (B), respectively.

(F) Snapshot images at the start (0) and after 15, 30, 45, or 60 min of time-lapse recording of 14-DIV tdT-labeled MHNs in control (top) or hypoxia (bottom) conditions. Solid arrowheads indicate spines with a persistent increase or decrease in length. Open arrowheads indicate spines that do not change their length. Each color denotes a distinct spine. The red asterisk indicates a sprouting dendrite.

(G and H) Length of protrusions at 0 and 1 hr of recording in normoxia or hypoxia (G, n ≥ 40) and distribution of spines according to length variation (H). Stable, Δ length ≤ 0.2 μm.

Data are mean ± SEM. ***p < 0.001. Scale bars, 10 μm (A–B′) and 5 μm (F). N, normoxia; H, hypoxia (1% O_2, A–E, or 0.5% O_2, F–H).

Also see Figures S1 and S2.

---

raised the question whether oxygen, via PHD2, might control actin-dependent spine formation. We thus investigated the role of PHD2 in the morphogenesis and maintenance of dendritic spines and synapses in hippocampal neurons.

RESULTS

Hypoxia and Dimethyl-Oxalylglycine Induce Immature Spines

In mouse hippocampal neurons (MHNs), dendritic spines emerge during 8–11 days in vitro (DIV) and progressively mature to shorter mushroom-shaped spines at 12–15 DIV, with concomitant induction of spontaneous synchronized network-wide spiking activity (Figures S1A–S1E). To evaluate whether physiological levels of hypoxia (which can be as low as 0.5% O_2 in the brain (Erecińska and Silver, 2001)) affect dendritic spine formation, 13-DIV MHNs were incubated overnight (o/n) in normoxia (21% O_2) or hypoxia (1% O_2). To visualize dendritic protrusions, we transfected 10-DIV MHNs with yellow (YFP) or tandem dimer tomato (tdT) fluorescent proteins. Neurons exposed to hypoxia showed reduced protrusion density, and most spines were

long filopodium-like protrusions without a head (Figures 1A–1E). Similar effects were seen in established mature spines when treatment started at 20 DIV (Figures S1F–S1J). These alterations were not due to changes in neuronal viability (Figures S1K–S1M) or oxidative stress (Figure S1N).

Time-lapse imaging of 14-DIV YFP-labeled MHNs for 1 hr showed that, in normoxia, 45% of the spines were stable in length (variations ≤ 0.2 μm), whereas the rest slightly increased or reduced their length (Figures 1F–1H). In hypoxia (0.5% O_2), most spines became longer or regressed, and only 33% kept their original length (Figures 1F–1H). Similar effects were observed upon o/n treatment of 13-DIV MHNs with the PHD inhibitor dimethyl-oxalylglycine (DMOG), which upregulates hypoxia-responsive genes and the HIF-dependent luciferase reporter (Figures S1O and S1P and S2A–S2I) without causing apoptosis or oxidative stress (Figures S1K–S1N). Neurons did not suffer irreversible damage because washout of DMOG restored spine density and maturation (Figures S2J–S2M′). Thus, inactivation of PHDs (by hypoxia or pharmacologic inhibition) impaired spine maturation, caused spine regression, and reduced spine density without altering viability.

Hypoxia and DMOG Induce Synaptic Impairment

To evaluate whether hypoxia and DMOG altered the electrophysiological properties of neurons, we performed patch-clamp recordings. 13- or 20-DIV MHNs were incubated o/n in normoxia or hypoxia or treated with DMOG. Neither hypoxia nor DMOG altered their passive electrical membrane properties (Figures S3A–S3C) or intrinsic excitability (Figures S3D–S3F), as confirmed by evoking antidromic action potentials (APs) upon repeated extracellular electrical stimulation (Figure S3G). These results show that hypoxia or DMOG did not change the ability of neurons to initiate and propagate APs upon stimulation. They did also not alter the time course of individual APs (Figures S3H–S3K). However, hypoxia and DMOG reduced the frequency of spontaneous AP firing (Figures 2A and 2B; Figure S3L), suggesting that MHNs had fewer functional synaptic connections and received less excitatory synaptic input.

We also explored whether the morphological changes of dendritic protrusions were reflected by functional alterations in synaptic transmission. Hypoxia and DMOG reduced excitatory synaptic transmission at 14 and 21 DIV, as evidenced by the suppressed spontaneous synchronized network-wide spiking activity (bursts), whereas inhibitory synapses were unaffected because not only burst duration but also burst frequency were reduced (Figures 2C and 2D; Figures S3M–S3O). Neurons recovered from hypoxia or DMOG and restored synchronized spiking activity 24 hr after switching back to control conditions (Figures 2C and 2D; Figures S3M–S3O), consistent with the morphological recovery after DMOG washout (Figures S2J–S2M′).

Immunostaining showed that hypoxia and DMOG reduced synaptic density, as assessed by the decreased co-localization of the presynaptic marker vGlut1 and the postsynaptic marker PSD-95 (Figures 2E–2H), or the density of the presynaptic marker synaptophysin (Figures S3P–S3S). However, no differences in the abundance or (plasma membrane) localization of the α-amino-3-hydroxy-5-methyl-4-isoxazolepropionic acid (AMPA) receptors GluA1 and GluA2 were detected (data not shown), indicating that the reduced excitatory signaling upon hypoxia or DMOG was not due to downregulation of postsynaptic AMPA receptors. Instead, the reduced synaptic transmission upon hypoxia or DMOG results from the remodeling of dendritic spines and the decreased synaptic density.

PHD2 Is Expressed in Hippocampal Neurons

To define which PHDs are involved, we analyzed the expression of PHDs. In situ hybridization, RT-PCR, and RNA sequencing (RNA-seq) revealed that *Phd1* (also known as *Egln2*) and *Phd2* (*Egln1*), but not *Phd3* (*Egln3*), were detected in the brain of mouse embryos or neonates (Figures S4A–S4C). In the adult brain, *Phd2* was detected in the hippocampus, cortical layers II, III, and V, and other regions (Figure S4A; data not shown). A low *Phd1* signal was detected in the hippocampus (Figure S4A).

We prepared postsynaptic density (PSD) fractions from 2-week-old wild-type (WT) mice (Cho et al., 1992). Protein enrichment was assessed by immunoblotting (IB) for PSD-95 and synaptophysin as post- and pre-synaptic markers, respectively. IB showed that PHD2 was broadly present, including in synaptosomes and PSDs (Figure 3A). Using an antibody specific for PHD2 in immunostainings (Figures S4D–S4H), PHD2 was detected in neurites and dendritic protrusions of MHNs (Figure 3B) and rat hippocampal neurons (RHNs) (data not shown), in close apposition to synaptophysin+ puncta, suggesting postsynaptic localization. A wide distribution was also obtained in MHNs transfected with YFP-tagged PHD2 (PHD2^{WT}YFP) (Figure S4I).

## *Phd2* Silencing Impairs Dendritic Spine Maturation

To assess whether PHD2 regulated spine formation, we silenced *Phd2* in MHNs. 7-DIV MHNs were co-transfected with YFP and control scrambled (scr) short hairpin RNA (shRNA) or *Phd2*-specific shRNA (shPhd2). At 14 DIV, *Phd2* silencing reduced dendritic protrusion density and the frequency of spines with a head, whereas it increased protrusion length (Figures 3C, 3D, and 3G–3I). Hypoxia did not further alter these parameters in *Phd2*-silenced MHNs (Figures 3E–3I). Time-lapse imaging showed that scr MHNs behaved as the control and retained most spines (Figures S4J–S4L, compare with Figures S2F–S2I, ctrl), whereas shPhd2 resembled DMOG-treated neurons with lower spine density and longer spines (Figures S4J–S4L). *Phd2* silencing did not alter passive and excitable electrical membrane properties, as recorded by patch-clamping, but reduced the frequency of the spontaneously fired APs (Figures S5A–S5J). *Phd2* silencing also impaired synaptic density, as revealed by the reduced number of vGlut1+/PSD-95+ co-clusters (Figures 3J–3L) and synaptophysin+ clusters (Figures S4M–S4Q). Silencing of *Phd1* did not affect spines (Figures S4R–S4T). Thus, PHD2 regulated the formation and maintenance of spines and synapses.

Loss of PHD2 Impairs Dendritic Spine Maturation

To confirm the shRNA results, we isolated MHNs from *Phd2*$^{lox/lox}$ embryos and transfected them at 7 DIV with the Brainbow1.0 (BBW) plasmid alone or together with a Cre recombinase (Cre) plasmid. BBW expresses red fluorescent protein (RFP) in the absence of Cre and CFP or YFP in the presence of Cre. Compared with control RFP+ neurons, YFP+ or CFP+ PHD2-deficient cells had reduced protrusion density and increased protrusion length (Figure S4U). Similar results were obtained in MNHs from mice lacking PHD2 in neurons (PHD2^{NKO}) (Figures 3M–3Q; Figure S4V). Also, PHD2 deletion reduced the frequency and synchronicity of spontaneous bursts of APs (Figure 3R; Figure S5K). The phenotype of PHD2^{NKO} spines was rescued by PHD2^{WT}YFP but not by an inactive PHD2 mutant that lacks hydroxylation activity (PHD2^{MUT}YFP) (Vogel et al., 2010; Figure 3S; Figures S4W–S4Y). Thus, PHD2-mediated hydroxylation is required to induce dendritic spine maturation.

Phd2 Regulates Dendritic Spine and Synaptic Density In Vivo

To evaluate the effect of *Phd2* silencing on dendritic spines in vivo, we performed shRNA knockdown of *Phd2* by in utero electroporation of the hippocampus in embryonic day 15.5 (E15.5) embryos (Pacary et al., 2012) with a bigenic vector co-expressing the shRNA and ZsGreen1 fluorescent protein. Analysis of dendritic spines in the hippocampal CA1 region on postnatal day 15 (P15) revealed that spine density was reduced in shPhd2 neurons in vivo (Figure 3T; Figures S6A and S6B).
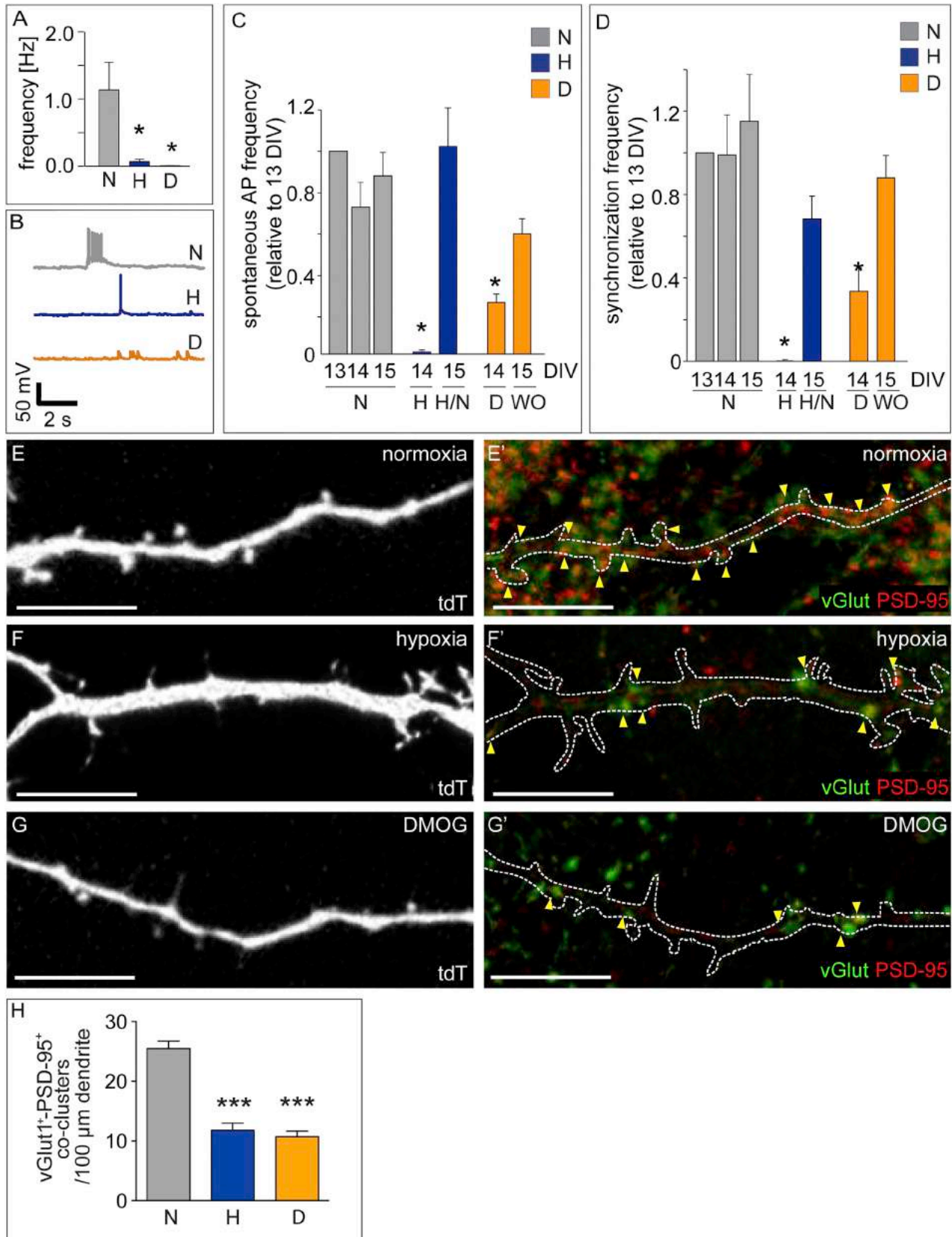
(legend on next page)

Golgi staining showed that spine density was reduced in PHD2^{NKO} mice (Figures S6C–S6E). To gain insight into the role of PHD2 in synapse formation in vivo, we analyzed the stratum radiatum of the hippocampal CA1 region. Transmission electron microscopy (TEM) and immunostaining revealed that PHD2^{NKO} littermates had reduced synaptic density (Figures S6F and S6G) (number of synapses/100 μm^2, 38.98 ± 0.90 for control (ctrl) versus 32.95 ± 1.17 for PHD2^{NKO}; n = 3 animals; p < 0.001) and synaptophysin$^+$ and PSD-95$^+$ signals (Figures S6H–S6M). Thus, PHD2 regulates spine morphogenesis and synaptic density in vivo.

Hypoxic Spine Remodeling Occurs Prior to HIF-Mediated Transcription

To identify the molecular mechanism by which PHD2-mediated hydroxylation regulated spine morphogenesis, we explored the involvement of HIF-1α. We evaluated the kinetics of HIF-mediated transcription after PHD blockade by using the 9xHRE::Luciferase reporter. Luciferase (Luc) activity was increased, but only after 20 hr of hypoxia or DMOG, and the blocker acriflavine abolished this effect (Figure S1P). Thus, HIF-mediated transcription occurred later than the onset of spine remodeling, suggesting an HIF-independent mechanism. Also, hypoxia still induced dendritic spine changes in HIF-1α^{NKO} MHNs (obtained by transducing MHNs from *Hif-1α*$^{lox/lox}$ mice with an adenoviral Cre vector; data not shown), further indicating that spine remodeling occurred independently of HIF-1α.

FLNA Is Expressed in Dendritic Filopodia and Spines

We considered alternative targets for PHD2 and focused on the actin cross-linker FLNA because it interacts with VHL (Tsuchiya et al., 1996), thus providing a putative molecular link between the cytoskeleton and hypoxia. FLNA is detected in the soma and dendrites, although its localization in spines is debated (Nestor et al., 2011; Noam et al., 2012). Staining of RHNs with a specific anti-FLNA antibody (Figures S7A and S7B) used in conjunction with confocal imaging confirmed that FLNA was detectable in the soma and dendrites and in structures resembling dendritic spines, close to synaptophysin$^+$ clusters (data not shown). To enhance spatial resolution of FLNA$^+$ puncta, we used high-resolution structured illumination microscopy (SIM), which showed FLNA$^+$ puncta in filopodium-like protrusions and the head of mature dendritic spines (Figure 4A; Figures S7C and S7D). The use of SIM and YFP-transfected neurons at 14 DIV, when spines are still remodeling, may explain the more prominent detection of FLNA in spines compared with other studies using conventional resolution microscopy of untransfected neurons (which makes precise spine visualiza-

tion more challenging) at 3–4 weeks in culture, when spines and synapses are mature and stable (Noam et al., 2012; Nwabuisi-Heath et al., 2012).

To confirm the localization of FLNA, we transfected MHNs with Turquoise2 (TQ2)-tagged FLNA (FLNA^{FL}TQ2). In normoxia, FLNA^{FL}TQ2 was detected in the somato-dendritic compartment, especially in the heads of mature dendritic spines (Figure 4B). In hypoxia, FLNA^{FL}TQ2 was more widespread in the entire neuron, including in filopodia (Figure 4B). The C terminus part of FLNA (FLNA^{CT}TQ2), which does not bind actin, showed widespread distribution in MHNs independent of oxygen levels (Figure S7E). To provide biochemical confirmation, we prepared PSD fractions. FLNA was detected in all fractions, notably in the PSDs (Figure 4C; Figure S7F). Exposure of mice to hypoxia (8% O$_2$) for 4 hr (a procedure upregulating HIF target genes; Figure S7G) altered FLNA levels and/or distribution (Figure 4C; Figure S7F). FLNA was especially increased in the non-synaptosomal membrane fraction (Figure 4C; Figure S7F). Thus, FLNA was detectable in dendritic spines and PSDs of neurons, and its localization and levels were influenced by hypoxia.

FLNA Is Stabilized by Hypoxia, DMOG, or PHD2 Knockdown

Hypoxia and DMOG regulated FLNA levels. Time-course studies in MHNs revealed that FLNA protein levels increased already within 15 min (for DMOG; data not shown) and remained elevated for several hours (Figures 4D and 4E; Figures S7H and S7I). This upregulation was independent of gene transcription or protein translation because *Flna* transcript levels were not induced during the first 4 hr (Figure S7J), and treatment of hypoxic MHNs with actinomycin D or cycloheximide did not prevent FLNA protein upregulation (Figure 4F; Figure S7K). However, FLNA was upregulated when normoxic MHNs were treated with the proteasomal inhibitor MG132 in a dose-dependent manner (Figures 4F and 4G; Figures S7K and S7L). The combination of hypoxia plus MG132 did not further elevate FLNA levels above those in hypoxia (data not shown), suggesting that hypoxia and proteasomal inhibition act via the same mechanism.

We transduced MHNs with scr or shPhd2 lentiviral vectors. IB revealed that *Phd2* silencing increased FLNA levels (Figure 4H; Figure S7M). FLNA levels were also higher in homogenates and non-synaptosomal fractions of PHD2^{NKO} brains (Figure 4I; Figures S7N–S7S). Thus, oxygenation and PHD2 regulated FLNA protein levels via a mechanism involving proteasomal degradation.

Figure 2. Synaptic Activity and Density of MHNs in Hypoxia and DMOG

(A) Spontaneous AP firing recorded from single cells by patch-clamp.

(B) Representative APs recorded by patch-clamp.

(C and D) Frequency of spontaneous AP firing (C) and network-wide AP synchronization (D) (n = 4 MEAs/condition) in MHNs in the indicated conditions.

(E–G′), vGlut (green) and PSD-95 (red) immunostaining (E′–G′) of tdT-transfected MHNs (E–G) that were subjected at 20 DIV for 16 hr to the indicated conditions. The contours of the dendrites in (E)–(G) are indicated in (E′)–(G′).

(H) Quantification of dendritic density of vGlut$^+$/PSD-95$^+$ co-clusters (n ≥ 20 neurons) by counting the green and red co-clusters colocalizing or in immediate apposition with the dendrite/spine.

Data are mean ± SEM. *p < 0.05 versus normoxia (A) or versus their respective 13-DIV value (C and D). ***p < 0.001. Scale bars, 10 μm. H, hypoxia (1% O$_2$); H/N, hypoxia o/n followed by 24 hr of normoxia; D, DMOG (250 μM for A, B, G, and G′ and 1 mM for C and D); WO, washout.

Also see Figure S3.
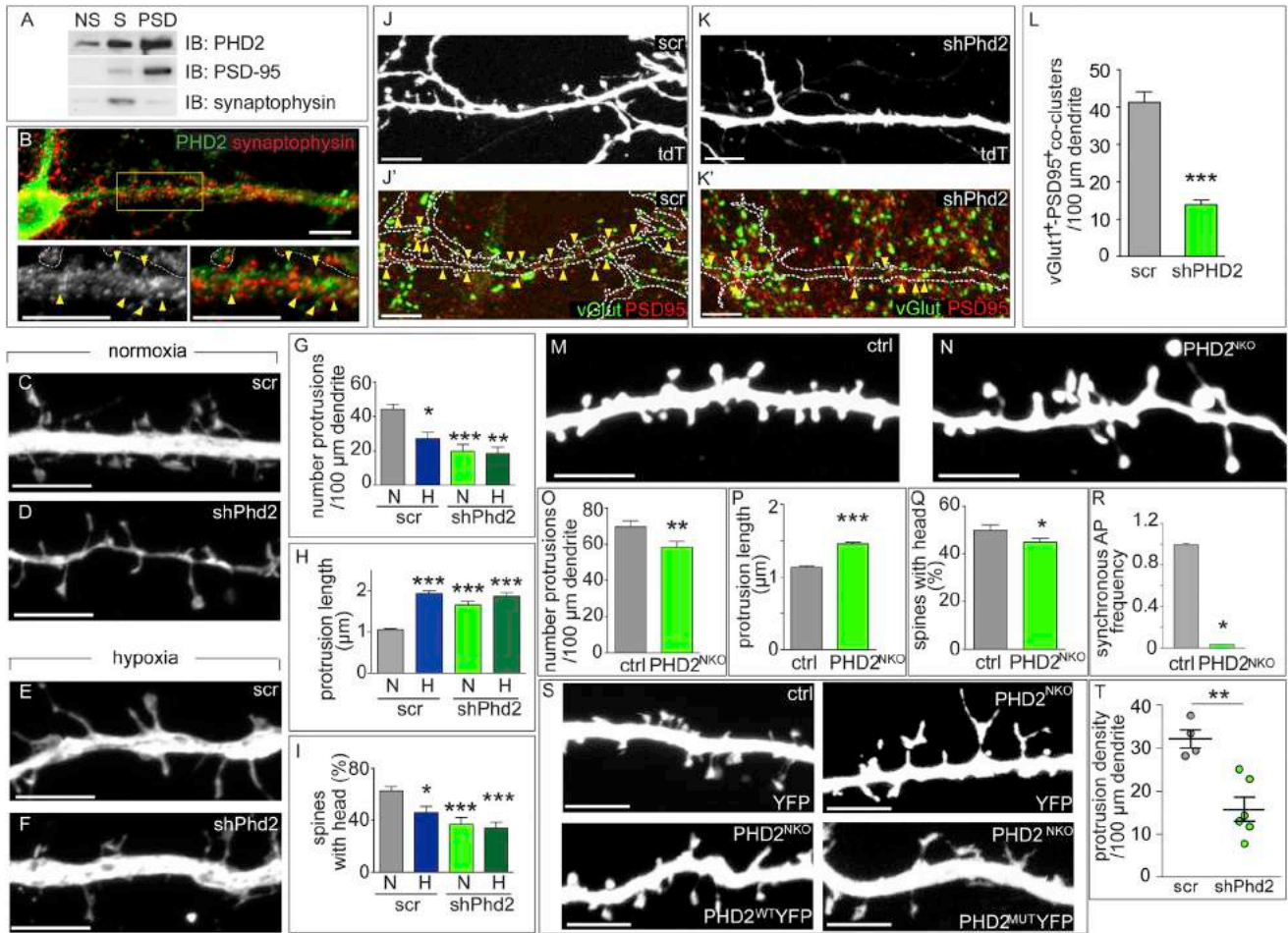
Figure 3. PHD2 Expression and Silencing in Dendritic Spines

(A) Representative IB of non-PSD fraction (NS), synaptic membranes (S), and PSD-enriched fractions for the indicated proteins.

(B) Staining of MHNs for PHD2 (green) and synaptophysin (red). The bottom panels are higher magnifications (bottom left: PHD2^{+} signal; bottom right: merged signal). Arrowheads indicate PHD2^{+} postsynaptic clusters. Dotted lines indicate neighboring cells (high-density cultures were used to maintain neurons in culture for prolonged periods). Green/red dots outside of the soma and dendrite are stainings of neighboring cells.

(C–I) 13-DIV MHNs co-transfected with YFP plus control shRNA (scr) (C and E) or shPhd2 (D and F) were incubated for 16 hr in normoxia (C and D) or hypoxia (E and F) and analyzed for protrusion density (G), protrusion length (H), and percent of spines with a head (I) (n = 3 experiments, 21–30 neurons, 300–1,400 protrusions).

(J–K') vGlut (green) and PSD-95 (red) immunostaining (J' and K') of MHNs co-transfected at 14 DIV with scr (J and J') or shPhd2 (K and K') together with tdT (J–L'). The contours of the dendrites in (J) and (K) are indicated in (J') and (K'), respectively.

(L) Quantification of dendritic density of vGlut[+]/PSD-95^{+} co-clusters (n ≥ 20 neurons).

(M–Q), YFP-transfected 14-DIV MHNs isolated from control (M) or PHD2[NKO] (N) littermates and analyzed for protrusion density (O), protrusion length (P), and number of spines with a head (Q) (n = 6 animals, >30 dendrites, >1,000 protrusions).

(R) Frequency of spontaneous network-wide AP synchronization (n = 4 MEAs/condition) of 14-DIV MHNs isolated from ctrl or PHD2[NKO] littermates.

(S) Representative dendritic protrusions of 14-DIV MHNs isolated from ctrl or PHD2[NKO] littermates upon transfection at 7 DIV with YFP (top), PHD2[WT]YFP (bottom left), or PHD2[MUT]YFP (bottom right).

(T) Analysis of dendritic protrusion density in the CA1 region of 2-week-old WT mice upon in utero electroporation at E15.5 with control shRNA (scr) or shPhd2 (n = 4–6 animals).

Data are mean ± SEM (G–I, L, and O–R) or single data plus mean ± SEM (T). *p < 0.05, **p < 0.01, ***p < 0.001. Scale bars, 10 μm (B) and 5 μm (C–F, J–K', M, N, and S).

Also see Figures S4–S6.

PHD2 Interacts with Domains D21–D23 of FLNA

Prompted by the similarities between the regulation of FLNA and HIF-1α by the PHD2/proteasome axis (Epstein et al., 2001), we hypothesized that FLNA was a target of PHD2-mediated proline hydroxylation and that hydroxylated FLNA underwent ubiquitination and proteasomal degradation. We first tested whether FLNA interacted with PHD2. We co-transfected HEK293T cells with myc-tagged FLNA (mycFLNA[FL]) and PHD2[WT]YFP or

PHD2^{MUT}YFP. Co-immunoprecipitation (coIP) showed that PHD2^{WT}YFP and PHD2^{MUT}YFP interacted with mycFLNA^{FL} (Figure 5A). FLNA and PHD2 also formed a complex in brain PSDs but not in the non-synaptic fraction (Figure 5B; Figure S8A).

FLNA contains an actin binding domain (ABD), 24 immunoglobulin G (IgG) domains (D1–D24), and two flexible regions (hinges H1 and H2) (Stossel et al., 2001; Zhou et al., 2010). To analyze which domains of FLNA interacted with PHD2, we generated five myc-tagged deletion variants of FLNA lacking domains known to interact with different binding partners (Zhou et al., 2010; Figure 5C). Proper folding of the FLNA variants was confirmed because mycFLNA^{NT} and mycFLNA$^{D12–D20}$ mutants bound to F-actin (data not shown), and mycFLNA^{CT} and mycFLNA$^{H2–D24}$ mutants (comprising the D24 dimerization domain) interacted with endogenous FLNA (Figure S8B). CoIPs showed that PHD2^{WT}YFP and PHD2^{MUT}YFP interacted with the deletion mutants mycFLNA^{CT} and mycFLNA$^{D21–D23}$ but not with other domains (Figure 5C; Figure S8C; data not shown). Complex detection was enhanced when using PHD2^{MUT}YFP, suggesting that they were stabilized in the absence of hydroxylation (Figure S8C).

We confirmed the PHD2-FLNA interaction by using fluorescence lifetime imaging microscopy (FLIM) to map the fluorescence resonance energy transfer (FRET) between the donor FLNA^{CT}TQ2 and the acceptor PHD2-YFP (using YFP as a control). Co-expression of FLNA^{CT}TQ2 and YFP did not change the fluorescence lifetime of the donor (Figure 5D). In contrast, co-expression of FLNA^{CT}TQ2 and PHD2^{WT}YFP increased FRET, as evidenced by the reduced TQ2 fluorescence lifetime (Figure 5D), indicating that they formed a complex in the range of 1–10 nm. Similar results were obtained when using PHD2^{MUT}YFP (Figure 5D). Thus, amino acid residues 2250–2508 in FLNA were necessary for FLNA-PHD2 binding, but the hydroxylation activity of PHD2 per se was not required.

PHD2 Hydroxylates Proline Residues P2309 and P2316 in FLNA

Although PHDs hydroxylate prolines in HIF-1α by recognizing an LXXLAP motif, other PHD targets lack such a motif (Wong et al., 2013). The mycFLNA$^{D21–D23-WT}$ fragment contains 20 prolines but none in an LXXLAP motif (Figure S8D). We examined the ability of each proline to interact with PHD2 by generating glutathione S-transferase (GST) fusion peptides, each containing a proline together with six up- and downstream flanking residues (Song et al., 2013). GST fusion peptides were incubated with homogenates of HEK293T cells expressing PHD2^{MUT}YFP. IB of precipitated complexes revealed that only peptides containing the prolines P2270, P2309, P2316, P2320, P2404, and P2439 interacted with PHD2 (Figure S8E). A weaker interaction was observed with peptides containing P2294 and P2312.

To analyze whether PHD2 hydroxylated FLNA prolines, we used an antibody specific for hydroxylated prolines (OH-Pro). HEK293T cells were transfected with mycFLNA^{FL} and treated with the proteasomal inhibitors MG132 or lactacystin, showing that proteasome inhibition increased FLNA hydroxylation (Figure 5E; Figure S8F). FLNA was also hydroxylated in vivo, and hydroxylation was reduced in rats exposed to hypoxia (8% O$_2$; Figure 5F).

To identify which prolines were hydroxylated by PHD2, we transfected HEK293T cells with plasmids encoding mycFLNA$^{D21–D23-WT}$ alone or together with PHD2^{WT}YFP. Cells were treated with vehicle or MG132, and immunoprecipitated mycFLNA$^{D21–D23-WT}$ was digested for liquid chromatography-mass spectrometry (LC-MS). Basal levels of OH-Pro of mycFLNA$^{D21–D23-WT}$ were detected in transfected cells. Hydroxylation of residues P2309, P2312, and P2316 in FNEE-HIP*DSP*FVVP*VASPSGDAR (P*: OH-Pro) were enhanced in double-transfected cells. The probability of hydroxylation was P2316 > P2309 > P2312, identifying P2316 and P2309 as the most probable PHD2 hydroxylation sites (Figure 5G; Figure S8G; data not shown).

We also mutated P2309 and P2316 to alanine (mycFLNA$^{D21–D23-P2309A}$, mycFLNA$^{D21–D23-P2316A}$) and tested their binding to PHD2 and hydroxylation upon co-transfection with PHD2^{WT}YFP. Although both sequence mutants interacted with PHD2^{WT}YFP, they were less hydroxylated than mycFLNA$^{D21–D23-WT}$ (Figure 5H; Figure S8H). Moreover, in the presence of DMOG, hydroxylation of mycFLNA$^{D21–D23-WT}$ was reduced to levels obtained with both sequence mutants (Figure 5H; Figure S8H), suggesting that PHD2 contributes to FLNA hydroxylation at P2309 and P2316.

VHL Regulates FLNA Protein Levels

VHL ubiquitinates hydroxylated HIFα to mark it for proteasomal degradation (Ivan et al., 2001; Jaakkola et al., 2001). Because FLNA interacts with VHL (Tsuchiya et al., 1996), and VHL was present in the PSDs (Figure 4C), we explored whether VHL mediated FLNA ubiquitination. We first validated the interaction between VHL and FLNA in MG132-treated HEK293T cells cotransfected with HA-tagged VHL (HA-VHL) and mycFLNA^{FL} (Figure 6A). FLNA deletion mutants showed that VHL bound to mycFLNA^{CT} and mycFLNA$^{D21–D23-WT}$ (Figure 6B; data not shown for mycFLNA^{NT} and mycFLNA$^{D11–D20}$). The single mutants mycFLNA$^{D21–D23-P2309A}$ and mycFLNA$^{D21–D23-P2316A}$ were still able to interact with VHL, whereas the triple mutant P2309/2312/2316A (mycFLNA$^{D21–D23-3P→A}$) showed a weaker interaction (Figure 6C; Figure S9A). Taken together, our results suggest that hydroxylation of P2309, P2316, and possibly P2312 was required for the interaction of FLNA with VHL.

We then evaluated whether Vhl silencing increased FLNA levels. Transduction of MHNs with a lentivirus expressing scr or Vhl-specific shRNA (shVhl, reducing VHL levels by 67% ± 4%; n = 3; p < 0.05) showed higher FLNA protein levels in VHL-silenced neurons (Figure 6D). To confirm that VHL regulates FLNA levels in vivo, we generated VHL^{NKO} mice by crossing Vhl$^{lox/lox}$ mice with NestinCre mice. Because these mice are lethal at E16.5, we made brain homogenates from E14.5 control or VHL^{NKO} littermates. As expected, HIF-1α levels were increased in VHL^{NKO} embryos (Figure 6E). Notably, FLNA levels were higher in VHL^{NKO} mice (Figure 6E; Figure S9B). We analyzed whether VHL deficiency increased the levels of hydroxylated FLNA. Because protein abundance in E14.5 embryo brains was insufficient for IP, E14.5 VHL^{NKO} brain extracts were blotted for OH-Pro and reblotted thereafter for FLNA. This analysis showed that the increased FLNA levels were comparably hydroxylated in VHL^{NKO} mice
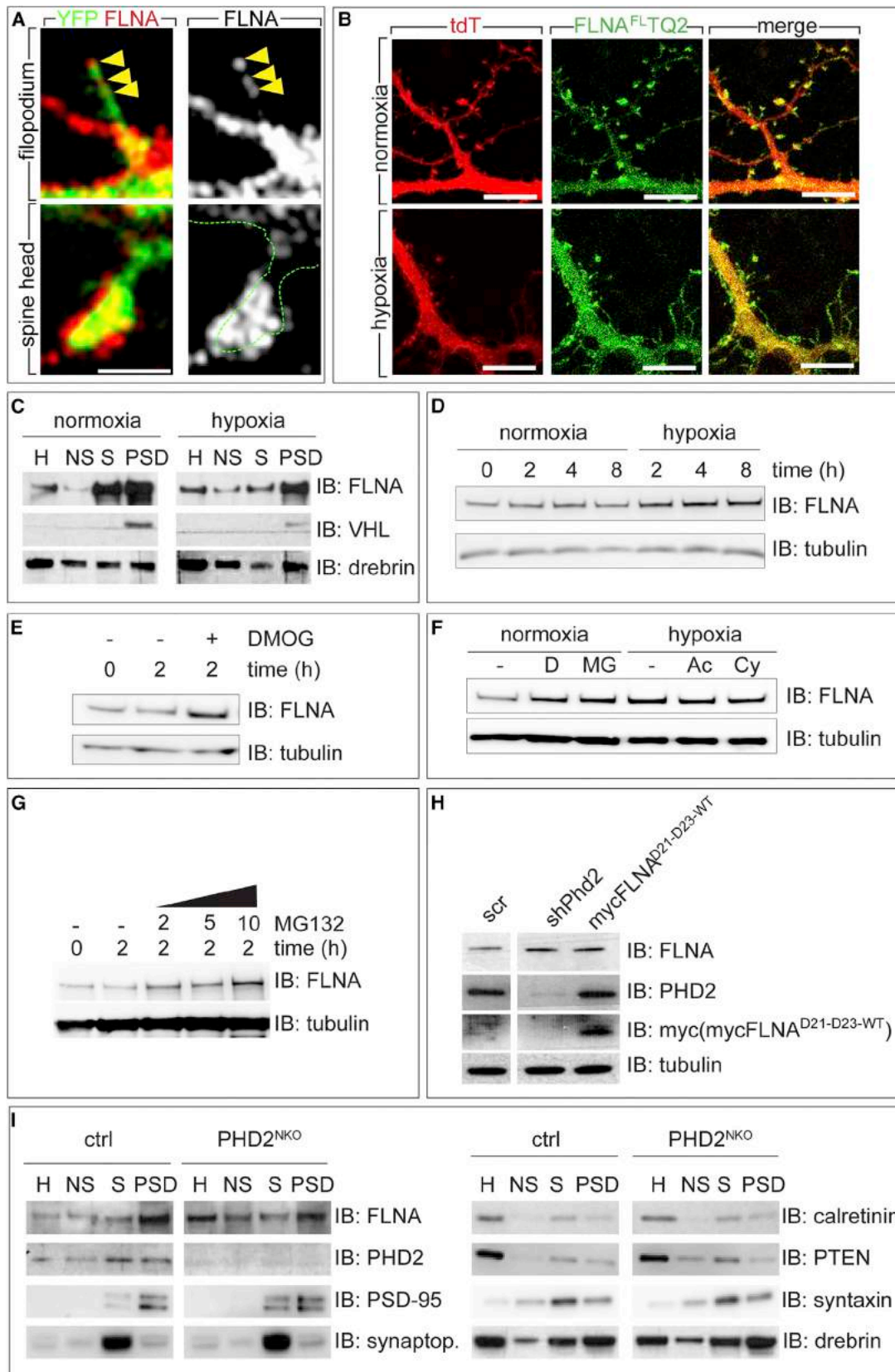
(legend on next page)

(Figure 6F; Figures S9C–S9E), suggesting that proline-hydroxylated FLNA was stabilized in the absence of VHL in vivo.

VHL Ubiquitinates FLNA

We then assessed whether the interaction of hydroxylated FLNA with VHL resulted in FLNA ubiquitination. Brains from E14.5 VHL[NKO] and control littermates were collected in the presence of MG132 and PR-619. Tandem ubiquitin binding entities (TUBE) pull-down of poly-ubiquitinated proteins followed by IB showed that FLNA was ubiquitinated less in VHL[NKO] brains (Figure 6G; Figure S9F).

FLNA Levels Determine Dendritic Spine Morphology

We assessed whether FLNA stabilization was responsible for the remodeling of dendritic spines to a more immature state. Because forced overexpression of full-length FLNA was toxic (data not shown), we used another strategy to elevate endogenous FLNA to physiological levels. We took advantage of the observation that overexpression of mycFLNA[D21–D23-WT] increased the levels of endogenous FLNA 2-fold (Figures 4H and 7A; Figure S7M), akin to the effect of hypoxia, DMOG, or Phd2 silencing (Figures 4D–4F, 4H, and 7A; Figures S7H, S7I, S7K, and S7M). FLNA[D21–D23-WT] elevated FLNA levels by impairing the interaction between endogenous FLNA and PHD2 because less PHD2 was coimmunoprecipitated with mycFLNA[FL] in the presence of GST-FLNA[D21–D23-WT] (Figure 7B). We therefore tested whether mycFLNA[D21–D23-WT] expression, and concomitant elevated FLNA levels, impaired dendritic spine maturation. MHNs transfected with mycFLNA[D21–D23-WT] had fewer and less mature dendritic spines (Figures 7C, 7D, and 7F–7H) and formed fewer synaptic contacts (Figures 7I–7L), comparable with the response to hypoxia (hypoxia versus mycFLNA[D21–D23-WT], p > 0.05 for all parameters; data not shown).

Because FLNA also interacts with Rac and Cdc42, which promote mature spine formation (Nakamura et al., 2011; Tashiro and Yuste, 2004), a possible dominant-negative interaction of mycFLNA[D21–D23-WT] with these small GTPases might also contribute to the more immature spine phenotype of mycFLNA[D21–D23-WT]-expressing neurons. To assess the specificity of this peptide in mediating the PHD2-regulated FLNA degradation, we used the mycFLNA[D21–D23-3P→A] mutant.

Notably, this mutant failed to impair spine maturation and synaptic contact formation (Figures 7E–7H, 7K, and 7L). Although we cannot formally exclude that mycFLNA[D21–D23-WT] perturbs the interaction with other binding partners of FLNA, the lack of an effect by mycFLNA[D21–D23-3P→A] strongly suggests that the effect of mycFLNA[D21–D23-WT] on spine morphology was due to its interaction with PHD2/VHL and to FLNA degradation rather than to non-specific dominant-negative interactions with other proteins. Notably, 14-DIV MHNs of E15.5 VHL[NKO] mice (containing higher levels of endogenous FLNA) also showed more immature dendritic spines (Figures S9G and S9H).

We explored whether Flna silencing reverted the phenotype induced by silencing Phd2. We co-transfected MHNs with tdT together with scr or Flna-specific shRNA (shFlna) alone or together with shPhd2. shFlna reduced FLNA protein levels by 59% ± 8% (n = 3, p < 0.05). Silencing of Flna in MHNs alone increased protrusion length without affecting the protrusion density or the number of spines with a head (Figures 7M–7S). However, in Phd2-silenced MHNs, Flna silencing largely prevented the switch to a more immature spine phenotype (Figures 7M–7S). Thus, FLNA is required for the spine morphology changes induced by PHD2 knockdown.

DISCUSSION

Adaptation of Dendritic Spines to Hypoxia

Our study shows that oxygen, via PHD2, regulates dendritic spines and synaptic transmission. PHD2 coordinates rapid, reversible adaptations of spines, at least in part, by controlling FLNA levels. When oxygen is limited, PHD2 is inactivated, which diminishes proteasomal degradation of FLNA, thus inducing its stabilization and accumulation in non-synaptic locations and increasing the ratio of FLNA to F-actin. Based on reports in other cells (van der Flier and Sonnenberg, 2001), we speculate that the increased FLNA abundance results in remodeling of the actin cytoskeleton from a mesh network in mature spine heads to parallel F-actin bundles in headless immature elongated protrusions.

Our data suggest that diminished degradation of FLNA upon PHD2 inactivation in hypoxia rearranges the actin cytoskeleton to reduce the number of dendritic spines, synapses, and synaptic transmission without affecting intrinsic electrical

---

Figure 4. Filamin A Expression in Dendritic Spines

(A) SIM micrograph of YFP[+] (green) RHNs immunostained for endogenous FLNA (red; gray at the right). Arrowheads indicate FLNA[+] puncta in filopodium (top). The green dashed line indicates the contour of a dendritic spine head (bottom).

(B) 14-DIV MHNs co-transfected with tdT (red) and FLNA[FL]TQ2 (green) in normoxia or hypoxia.

(C) Representative IB for FLNA, VHL, and drebrin of mouse brain homogenate (H), non-synaptic fraction (NS), synaptic membranes, and PSD-enriched fractions from WT mice exposed to normoxia or hypoxia (8% O$_2$) for 4 hr.

(D) Representative IB for FLNA and tubulin in 14-DIV MHNs subjected to normoxia or hypoxia for the indicated times.

(E) Representative IB for FLNA and tubulin in 14-DIV untreated MHNs or MHNs treated with DMOG for 2 hr.

(F) Representative IB for FLNA and tubulin in untreated MHNs (−) or treated with DMOG (D), MG132 (MG), actinomycin D (Ac), or cycloheximide (Cy) in normoxia or hypoxia.

(G) Representative IB for FLNA and tubulin in MHNs treated for 2 hr with increasing concentrations of MG132.

(H) IB for FLNA, PHD2, myc, and tubulin in MHNs transduced with scrambled control shRNA, shPhd2, or overexpressing mycFLNA[D21–D23-WT].

(I) Representative IB for the indicated proteins of mouse brain homogenate (H), non-synaptic fraction, synaptic membranes, and PSD-enriched fractions obtained from ctrl or PHD2[NKO] littermates.

Synaptop., synaptophysin. Densitometry of IBs as shown in (C)–(I) is shown in Figure S7. Scale bars, 1 μm (A) and 10 μm (B).

Also see Figure S7.
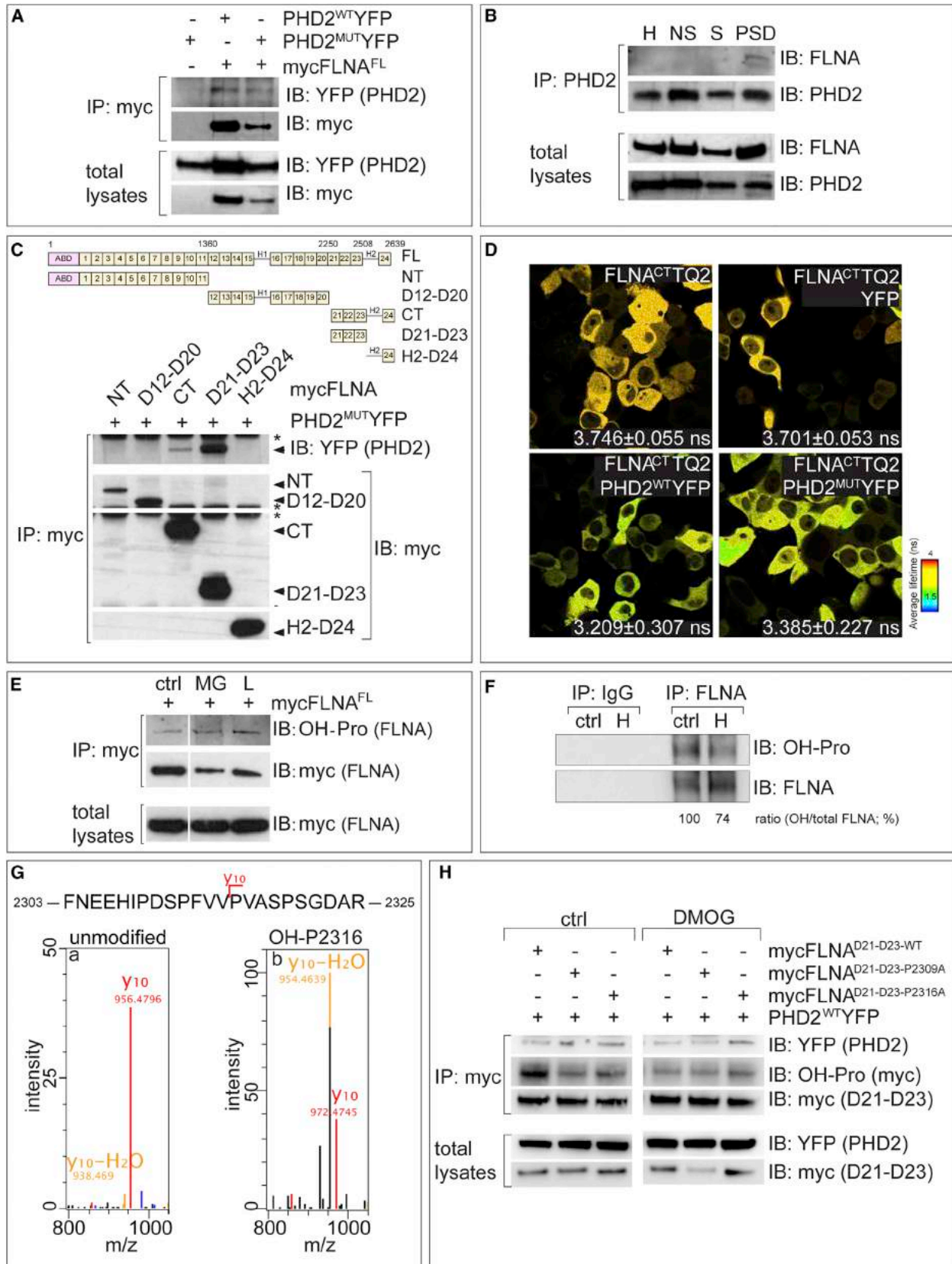
(legend on next page)

membrane properties. Our findings are in line with a report showing that chemical inhibition of PHDs and PHD2 deficiency reduce long-term potentiation (Corcoran et al., 2013). Experiments targeting FLNA[D21–D23] to dendritic spines by using a spine-targeting domain (such as of SG2NA; Gaillard et al., 2006) to inhibit PHD2 locally in the spines could be designed to confirm the model that PHD2 activity, locally at the spines, mediates spine maturation.

PHD2 Targets FLNA for Proteasomal Degradation

PHDs orchestrate the levels of target proteins via hydroxylation of prolines, although hydroxylation-independent activities have also been reported (Wong et al., 2013). Using a combination of biochemical, imaging, and site-directed mutagenesis methods, we show that PHD2 interacts with domains D21–D23 of FLNA and hydroxylates P2309 and P2316 (conserved in zebrafish, mouse, rat, and human), favoring its ubiquitination and proteasomal degradation. This FLNA/PHD2/VHL machinery is present in PSDs of dendritic spines. Inactivation of PHD2 hydroxylation activity or mutation of P2309 and P2316 to alanine impaired FLNA hydroxylation. Triple mutation of P2309, P2312, and P2316 reduced the interaction with VHL. Genetic studies in vitro and in vivo confirmed the importance of PHD2 and VHL in dendritic spine remodeling. Together, these studies identify FLNA as a target of PHD2 involved in the formation and maturation of dendritic spines.

In immortalized cell lines, hypoxia induces FLNA cleavage (Zheng et al., 2014). However, hypoxia or DMOG did not upregulate such an FLNA fragment in MHNs (data not shown), perhaps because the effects of hypoxia on FLNA levels are cell-type dependent or differ upon immortalization. In any case, FLNA protein levels in primary MHNs were increased—not decreased—upon exposure to hypoxia or DMOG. Although spine remodeling by PHD2 is HIF-independent, we cannot exclude that other PHD2 targets, apart from FLNA, influence spine remodeling.

Precise Regulation of FLNA Levels

Somewhat counterintuitively, both the modest elevation of FLNA (by mycFLNA[D21–D23-WT]) and silencing of Flna resulted in similar—although not exactly identical—spine changes. Indeed, silencing of Flna increased protrusion length without affecting the protrusion density or the number of spines with a head, whereas MHNs transfected with mycFLNA[D21–D23-WT] had fewer and less mature dendritic spines. This apparent contradiction likely relates to the well-known fact that FLNA interacts with several partners and has contextual effects and that FLNA protein levels require precise regulation. Indeed, both under- and overexpression of FLNA impair neuronal migration, although via distinct molecular mechanisms (Sarkisian et al., 2006; Zhang et al., 2012, 2013). Furthermore, both loss and gain of FLNA/cheerio in humans and flies cause similar neurological defects, although distinct symptoms have also been reported (Bolduc et al., 2010; Zhou et al., 2010). All this suggests that FLNA protein levels must be tightly regulated in neurons. Our findings that FLNA is post-translationally regulated by PHD2-mediated hydroxylation and VHL-mediated ubiquitination unravel a molecular mechanism for the precise regulation of FLNA abundance, required for the proper formation and maintenance of synapses.

Physiological Relevance: A Hypothesis?

Our findings that hypoxia rapidly induces reversible spine regression may help to better understand how neurons adapt to a hypoxia challenge. Because synaptic transmission is a high-energy-consuming process and neurons rely on oxygen to produce ATP, one possible mechanism whereby neurons can avoid an energy crisis is by decreasing synaptic transmission through spine regression. Importantly, this remodeling is not irreversible (which would otherwise impair brain performance permanently), but PHD2/FLNA may provide a molecular mechanism for reversible spine maturation and re-establishment of synapses upon return to sufficient oxygen conditions. Although our study was not designed to provide direct proof for such a protective mechanism, previous reports support this hypothesis. First, when ATP production is compromised, dendritic arborization is impaired (Oruganty-Das et al., 2012). Second, both an increase in spine length and a rapid reversible

---

Figure 5. Analysis of Filamin A as a PHD2 Target

(A) Representative IB for YFP and myc after IP of mycFLNA[FL] from HEK293T cells co-expressing mycFLNA[FL] and PHD2[WT]YFP or PHD2[MUT]YFP. Total lysates are shown below.

(B) Representative IB for FLNA and PHD2 after IP of PHD2 in mouse brain homogenate, non-synaptic fraction, synaptic membranes, and PSD fractions. Total lysates are shown below.

(C) Top: diagrams of the domains of full-length (FL) and deletion constructs of FLNA. 1–24, IgG repeats; H1 and H2, hinges. Bottom: representative IB for myc and YFP after IP of myc-tagged FLNA deletion mutants co-expressed with PHD2[MUT]YFP in HEK293T cells. Arrows indicate myc-tagged proteins and PHD2[MUT]YFP. Asterisks indicate aspecific bands.

(D) Representative fluorescence lifetime images (FLIM) and life time measurements of FLNA[CT]TQ2 when transfected alone or in combination with YFP, PHD2[WT]YFP, or PHD2[MUT]YFP in HEK293T cells (mean ± SEM, n ≥ 50 cells).

(E) Representative IB for hydroxyprolines (OH-Pro) or myc after IP of mycFLNA[FL] from HEK293T cells transfected with mycFLNA[FL] and treated for 2 hr with MG132 or lactacystin (L). Total lysates are shown below.

(F) Representative IB and densitometric quantification for FLNA and OH-Pro after IP with control IgG (left) or specific antibodies for FLNA (right) of brain homogenates from P10 rats housed in ctrl or hypoxia chambers.

(G) MS/MS fragmentation spectra of unmodified (a, from control HEK293T cells) and hydroxylated (b, from PHD2[WT]YFP-transfected HEK293T cells treated with MG132 for 2 hr) P2316 in FNEEHIPDSPFVVPVASPSGDAR of FLNA, focusing on the fragment ion (y10), showing a mass shift of 16 Da upon hydroxylation. Complete spectra are shown in Figure S8G.

(H) Representative IB for the indicated proteins after IP of myc in HEK293T cells co-transfected with PHD2[WT]YFP together with mycFLNA[D21–D23-WT], mycFLNA[D21–D23-P2309A], or mycFLNA[D21–D23-P2316A] and subjected to ctrl (left) or DMOG (right) treatment. Total lysates are shown below.

Also see Figure S8.
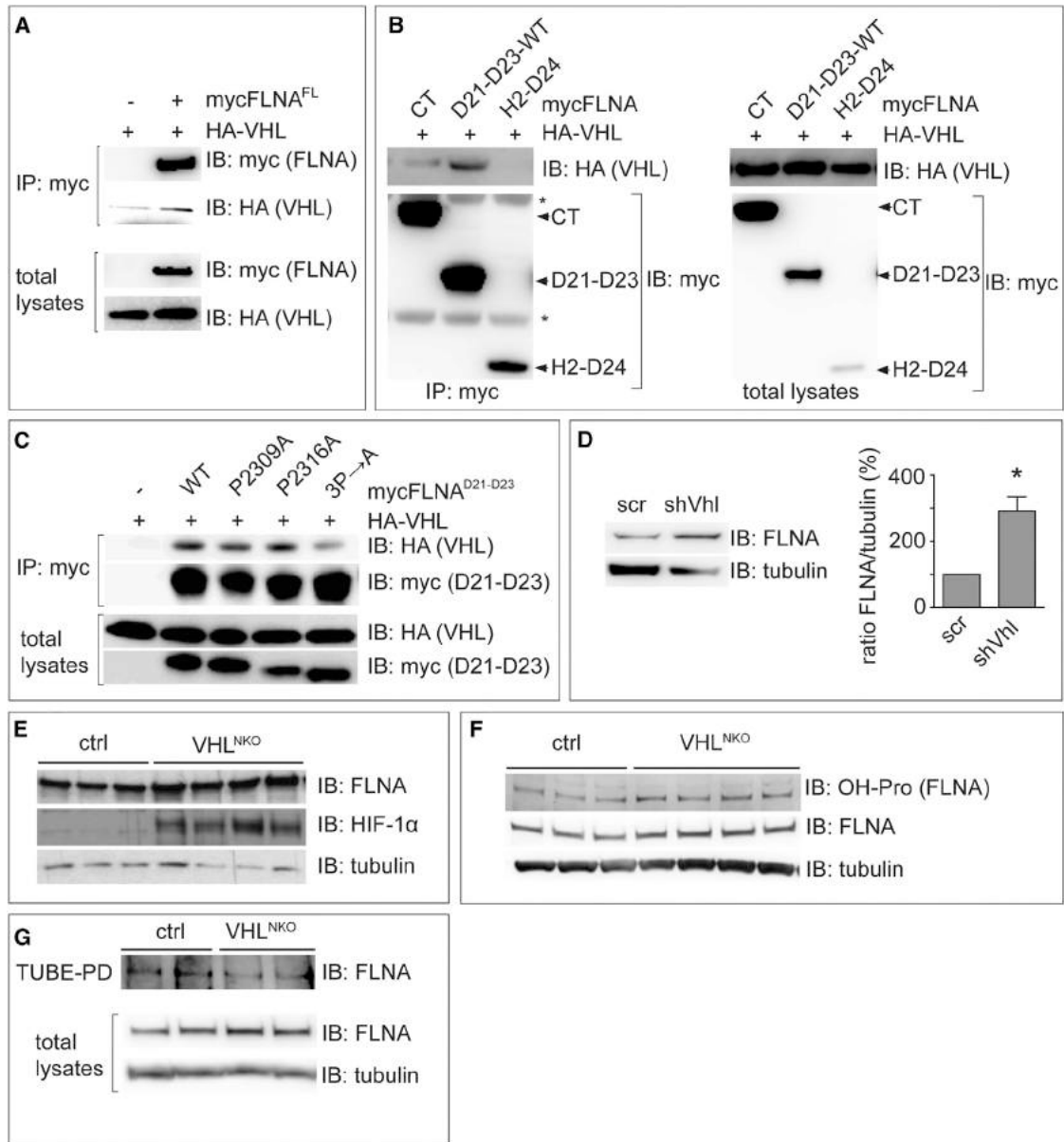
Figure 6. Analysis of Filamin A Interaction with VHL

(A) Representative IB for myc and HA after IP of myc from HEK293T cells transfected with mycFLNA^{FL} and HA-VHL. Total lysates are shown below.

(B) Representative IB for myc and HA after IP of myc from HEK293T cells transfected with mycFLNA^{CT}, mycFLNA$^{D21–D23-WT}$, or mycFLNA^{H2-D24} together with HA-VHL (left). Total lysates are shown (right). Arrowheads indicate myc-tagged proteins. Asterisks indicate IgGs used for the IP.

(C) Representative IB for myc and HA after IP of myc from HEK293T cells transfected with HA-VHL alone or co-transfected with mycFLNA$^{D21–D23-WT}$, mycFLNA$^{D21–D23-P2309A}$, mycFLNA$^{D21–D23-P2316A}$, or mycFLNA$^{D21–D23-3P→A}$ mutants. Total lysates are shown below.

(D) Representative IB for FLNA and tubulin in MHNs transduced with a control shRNA (scr) or shVhl (left). Also shown is densitometric quantification of FLNA protein levels (right, mean ± SEM, n = 3, *p < 0.05).

(E and F) Representative IBs for FLNA, HIF-1α, and tubulin (E) or for FLNA, hydroxyprolines (OH-Pro), and tubulin (F) of brain homogenates from E14.5 ctrl or VHL^{NKO} littermates.

(G) Representative IB for FLNA and tubulin after TUBE2 pull-down of brain homogenates obtained from E14.5 ctrl or VHL^{NKO} littermates. Total lysates are shown below.

Also see Figure S9.

spine retraction protect against excitotoxic damage in hypoxia (Araya et al., 2006; Meller et al., 2008). Third, in hypoperfused peri-infarct regions, neurons lower the number of mature spines and increase the length of protrusions to protect against excitotoxic overstimulation and to rewire new functional circuits (Brown et al., 2010).
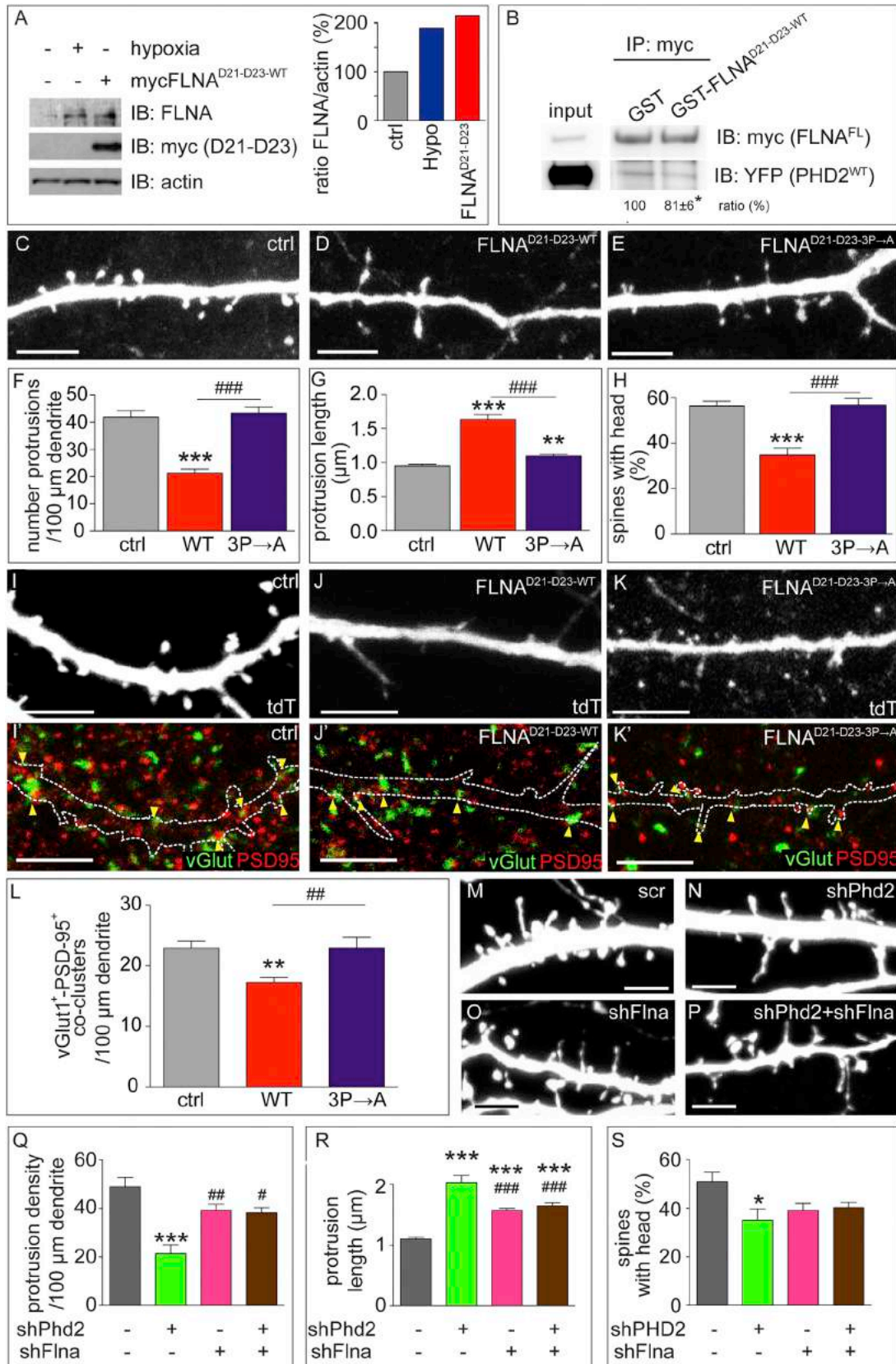
(legend on next page)

EXPERIMENTAL PROCEDURES

Detailed methods are described in the Supplemental Experimental Procedures.

Animals
Animal housing and procedures were approved by the Animal Ethics Committee of KU Leuven. We used Swiss, $Phd2^{lox/lox}$, PHD2^{KO}, *Nestin*Cre, $Vhl^{lox/lox}$, and Hif-$1\alpha^{lox/lox}$ mice and Wistar rats. In utero electroporations were performed at E15.5. Pups were exposed to 8% O_2 for 4 hr.

Cell Culture
Hippocampal neurons were isolated and cultured as described previously (Segura et al., 2007). Dendritic spines were analyzed at 14 DIV and synaptic densities at 21 DIV. HEK293T and rat PC12 cells were cultured as described. Hypoxic incubations were at 0.5%–1% (neurons) or 0.2% O_2 (HEK293T). Transfections were done by Lipofectamine 2000 (neurons), calcium phosphate (HEK293T), or Nucleofection (PC12). Transductions were done as described in the Supplemental Experimental Procedures.

RNA and Protein Analysis
Immunoblotting, immunoprecipitations, and pull-downs were done as described. RNA expression analysis was done by in situ hybridization, RT-PCR, or RNA-seq. Immunostaining was performed on 4% paraformaldehyde (PFA)-fixed hippocampal neurons or thick free-floating brain cryo- or vibratome sections.

Mass Spectrometry
HEK293T cells transfected with mycFLNA$^{D21-D23-WT}$ with or without PHD2^{WT}YFP were incubated with vehicle or 10 μM MG132 for 2 hr before lysis. Cell lysates were immunoprecipitated with anti-myc antibodies and fractionated by SDS-PAGE. The section containing mycFLNA$^{D21-D23-WT}$ was trypsinized in gel, and digested peptides were analyzed by nano-LC-MS/MS.

Imaging, Time Lapse, and Quantifications
Bright-field, fluorescent (time-lapse) confocal imaging, super-resolution imaging (SR-SIM), TEM, and time-domain FLIM were performed as described in the Supplemental Experimental Procedures. Morphometry (NIH ImageJ) was done blinded for the experimental conditions.

Cellular and Network Electrophysiology
Patch-clamp recordings in MHNs were performed as described previously (Reinartz et al., 2014). Extracellular recordings of the spontaneous network-level electrical activity, arising among neurons growing over multi-electrode arrays (MEAs), were performed as reported previously (Gambazzi et al., 2010).

Statistics
Experiments were performed at least three times. Data are expressed as mean ± SEM. Statistical differences were calculated by two-tailed unpaired t test for two datasets or ANOVA followed by Bonferroni post hoc test for multiple datasets using Prism (GraphPad). Statistical differences on data from MEAs were calculated by Wilcoxon rank-sum test. $p < 0.05$ was considered statistically significant.

SUPPLEMENTAL INFORMATION

Supplemental Information includes Supplemental Experimental Procedures and nine figures and can be found with this article online at http://dx.doi.org/10.1016/j.celrep.2016.02.047.

AUTHOR CONTRIBUTIONS

P.C. conceived the project. I.S., C.L., E.K., A.M., R.P., T.C., C.T., C.B., and B.G. performed the experiments and analyzed the data. I.S., C.L., E.K., A.M., R.P., G.E., T.C., C.T., M.M., B.G., M.G., C.R.A., M.D., and P.C. designed the experiments. D.D. and M.H. provided technical infrastructure, reagents, and expertise. I.S., C.L., M.D., and P.C. wrote the manuscript. All authors edited the paper.

REFERENCES

Araya, R., Jiang, J., Eisenthal, K.B., and Yuste, R. (2006). The spine neck filters membrane potentials. Proc. Natl. Acad. Sci. USA *103*, 17961–17966.

Figure 7. The Effect of Filamin A Upregulation on Spine Maturation

(A) Representative IB for FLNA, myc, and actin in HEK293T cells under control or hypoxia (0.2% O_2) conditions or after transfection with mycFLNA$^{D21-D23-WT}$ (left). Also shown is densitometric quantification of FLNA (right).

(B) Representative IB for myc and YFP after IP of myc in the presence of recombinant GST or GST-FLNA$^{D21-D23}$ proteins from homogenates of HEK293T cells co-transfected with mycFLNA^{FL} and PHD2^{WT}YFP. Left (input): total lysate control in co-transfected HEK293T cells. Densitometric quantification of the PHD2^{WT}YFP/mycFLNA^{FL} ratio is shown (n = 3, *p < 0.05).

(C–H), Representative images of tdT$^+$ 14-DIV ctrl (C), mycFLNA$^{D21-D23-WT}$ (D), or mycFLNA$^{D21-D23-3P\rightarrow A}$ (E) transfected MHNs. Also shown is quantification of protrusion density (F), protrusion length (G), and percentage of spines with a head (H) (n = 10 neurons, 324–731 protrusions).

(I–K′) Immunostaining of vGlut (green) and PSD-95 (red) (I′, J′, and K′) in 21-DIV tdT-transfected MHN (I–K) alone (I and I′) or together with mycFLNA$^{D21-D23-WT}$ (J and J′) or mycFLNA$^{D21-D23-3P\rightarrow A}$ (K and K′). The contours of the dendrites in (I), (J), and (K) are indicated in (I′), (J′), and (K′), respectively.

(L) Quantification of the dendritic density of vGlut$^+$/PSD-95$^+$ co-clusters (n ≥ 20 neurons).

(M–P) Representative images of 14-DIV MHNs co-transfected with tdT together with scrambled control shRNA (M), shPhd2 (N), shFlna (O), or both shPhd2 and shFlna (P).

(Q–S) Quantification of protrusion density (Q), protrusion length (R), and percentage of spines with a head (S) (n ≥ 7 neurons, 7–22 dendrites, 170–832 protrusions).

Data are mean ± SEM. *p < 0.05, ***p < 0.001 versus ctrl or scr. #p < 0.05, ##p < 0.01, ###p < 0.001 versus shPhd2 or mycFLNA$^{D21-D23-WT}$. Scale bars, 5 μm.

Bolduc, F.V., Bell, K., Rosenfelt, C., Cox, H., and Tully, T. (2010). Fragile x mental retardation 1 and filamin a interact genetically in Drosophila long-term memory. Front. Neural Circuits 3, 22.

Brown, C.E., Boyd, J.D., and Murphy, T.H. (2010). Longitudinal in vivo imaging reveals balanced and branch-specific remodeling of mature cortical pyramidal dendritic arbors after stroke. J. Cereb. Blood Flow Metab. 30, 783–791.

Cho, K.O., Hunt, C.A., and Kennedy, M.B. (1992). The rat brain postsynaptic density fraction contains a homolog of the Drosophila discs-large tumor suppressor protein. Neuron 9, 929–942.

Corcoran, A., Kunze, R., Harney, S.C., Breier, G., Marti, H.H., and O'Connor, J.J. (2013). A role for prolyl hydroxylase domain proteins in hippocampal synaptic plasticity. Hippocampus 23, 861–872.

Epstein, A.C., Gleadle, J.M., McNeill, L.A., Hewitson, K.S., O'Rourke, J., Mole, D.R., Mukherji, M., Metzen, E., Wilson, M.I., Dhanda, A., et al. (2001). C. elegans EGL-9 and mammalian homologs define a family of dioxygenases that regulate HIF by prolyl hydroxylation. Cell 107, 43–54.

Erecińska, M., and Silver, I.A. (2001). Tissue oxygen tension and brain sensitivity to hypoxia. Respir. Physiol. 128, 263–276.

Ethell, I.M., and Pasquale, E.B. (2005). Molecular mechanisms of dendritic spine development and remodeling. Prog. Neurobiol. 75, 161–205.

Gaillard, S., Bailly, Y., Benoist, M., Rakitina, T., Kessler, J.P., Fronzaroli-Molinières, L., Dargent, B., and Castets, F. (2006). Targeting of proteins of the striatin family to dendritic spines: role of the coiled-coil domain. Traffic 7, 74–84.

Gambazzi, L., Gokce, O., Seredenina, T., Katsyuba, E., Runne, H., Markram, H., Giugliano, M., and Luthi-Carter, R. (2010). Diminished activity-dependent brain-derived neurotrophic factor expression underlies cortical neuron microcircuit hypoconnectivity resulting from exposure to mutant huntingtin fragments. J. Pharmacol. Exp. Ther. 335, 13–22.

Hotulainen, P., and Hoogenraad, C.C. (2010). Actin in dendritic spines: connecting dynamics to function. J. Cell Biol. 189, 619–629.

Ivan, M., Kondo, K., Yang, H., Kim, W., Valiando, J., Ohh, M., Salic, A., Asara, J.M., Lane, W.S., and Kaelin, W.G., Jr. (2001). HIFalpha targeted for VHL-mediated destruction by proline hydroxylation: implications for O2 sensing. Science 292, 464–468.

Jaakkola, P., Mole, D.R., Tian, Y.M., Wilson, M.I., Gielbert, J., Gaskell, S.J., von Kriegsheim, A., Hebestreit, H.F., Mukherji, M., Schofield, C.J., et al. (2001). Targeting of HIF-alpha to the von Hippel-Lindau ubiquitylation complex by O2-regulated prolyl hydroxylation. Science 292, 468–472.

Mazzone, M., Dettori, D., Leite de Oliveira, R., Loges, S., Schmidt, T., Jonckx, B., Tian, Y.M., Lanahan, A.A., Pollard, P., Ruiz de Almodovar, C., et al. (2009). Heterozygous deficiency of PHD2 restores tumor oxygenation and inhibits metastasis via endothelial normalization. Cell 136, 839–851.

Meller, R., Thompson, S.J., Lusardi, T.A., Ordonez, A.N., Ashley, M.D., Jessick, V., Wang, W., Torrey, D.J., Henshall, D.C., Gafken, P.R., et al. (2008). Ubiquitin proteasome-mediated synaptic reorganization: a novel mechanism underlying rapid ischemic tolerance. J. Neurosci. 28, 50–59.

Nakamura, F., Stossel, T.P., and Hartwig, J.H. (2011). The filamins: organizers of cell structure and function. Cell Adhes. Migr. 5, 160–169.

Nestor, M.W., Cai, X., Stone, M.R., Bloch, R.J., and Thompson, S.M. (2011). The actin binding domain of βI-spectrin regulates the morphological and functional dynamics of dendritic spines. PLoS ONE 6, e16197.

Noam, Y., Phan, L., McClelland, S., Manders, E.M., Ehrengruber, M.U., Wadman, W.J., Baram, T.Z., and Chen, Y. (2012). Distinct regional and subcellular localization of the actin-binding protein filamin A in the mature rat brain. J. Comp. Neurol. 520, 3013–3034.

Nwabuisi-Heath, E., LaDu, M.J., and Yu, C. (2012). Simultaneous analysis of dendritic spine density, morphology and excitatory glutamate receptors during neuron maturation in vitro by quantitative immunocytochemistry. J. Neurosci. Methods 207, 137–147.

Oruganty-Das, A., Ng, T., Udagawa, T., Goh, E.L., and Richter, J.D. (2012). Translational control of mitochondrial energy production mediates neuron morphogenesis. Cell Metab. 16, 789–800.

Pacary, E., Haas, M.A., Wildner, H., Azzarelli, R., Bell, D.M., Abrous, D.N., and Guillemot, F. (2012). Visualization and genetic manipulation of dendrites and spines in the mouse cerebral cortex and hippocampus using in utero electroporation. J. Vis. Exp. 26, 4163.

Reinartz, S., Biro, I., Gal, A., Giugliano, M., and Marom, S. (2014). Synaptic dynamics contribute to long-term single neuron response fluctuations. Front. Neural Circuits 8, 71.

Sarkisian, M.R., Bartley, C.M., Chi, H., Nakamura, F., Hashimoto-Torii, K., Torii, M., Flavell, R.A., and Rakic, P. (2006). MEKK4 signaling regulates filamin expression and neuronal migration. Neuron 52, 789–801.

Segura, I., Essmann, C.L., Weinges, S., and Acker-Palmer, A. (2007). Grb4 and GIT1 transduce ephrinB reverse signals modulating spine morphogenesis and synapse formation. Nat. Neurosci. 10, 301–310.

Song, D., Li, L.S., Heaton-Johnson, K.J., Arsenault, P.R., Master, S.R., and Lee, F.S. (2013). Prolyl hydroxylase domain protein 2 (PHD2) binds a Pro-Xaa-Leu-Glu motif, linking it to the heat shock protein 90 pathway. J. Biol. Chem. 288, 9662–9674.

Stossel, T.P., Condeelis, J., Cooley, L., Hartwig, J.H., Noegel, A., Schleicher, M., and Shapiro, S.S. (2001). Filamins as integrators of cell mechanics and signalling. Nat. Rev. Mol. Cell Biol. 2, 138–145.

Tashiro, A., and Yuste, R. (2004). Regulation of dendritic spine motility and stability by Rac1 and Rho kinase: evidence for two forms of spine motility. Mol. Cell. Neurosci. 26, 429–440.

Tsuchiya, H., Iseda, T., and Hino, O. (1996). Identification of a novel protein (VBP-1) binding to the von Hippel-Lindau (VHL) tumor suppressor gene product. Cancer Res. 56, 2881–2885.

van der Flier, A., and Sonnenberg, A. (2001). Structural and functional aspects of filamins. Biochim. Biophys. Acta 1538, 99–117.

Vogel, S., Wottawa, M., Farhat, K., Zieseniss, A., Schnelle, M., Le-Huu, S., von Ahlen, M., Malz, C., Camenisch, G., and Katschinski, D.M. (2010). Prolyl hydroxylase domain (PHD) 2 affects cell migration and F-actin formation via RhoA/rho-associated kinase-dependent cofilin phosphorylation. J. Biol. Chem. 285, 33756–33763.

Wong, B.W., Kuchnio, A., Bruning, U., and Carmeliet, P. (2013). Emerging novel functions of the oxygen-sensing prolyl hydroxylase domain enzymes. Trends Biochem. Sci. 38, 3–11.

Zhang, J., Neal, J., Lian, G., Shi, B., Ferland, R.J., and Sheen, V. (2012). Brefeldin A-inhibited guanine exchange factor 2 regulates filamin A phosphorylation and neuronal migration. J. Neurosci. 32, 12619–12629.

Zhang, J., Neal, J., Lian, G., Hu, J., Lu, J., and Sheen, V. (2013). Filamin A regulates neuronal migration through brefeldin A-inhibited guanine exchange factor 2-dependent Arf1 activation. J. Neurosci. 33, 15735–15746.

Zhang, L., Bartley, C.M., Gong, X., Hsieh, L.S., Lin, T.V., Feliciano, D.M., and Bordey, A. (2014). MEK-ERK1/2-dependent FLNA overexpression promotes abnormal dendritic patterning in tuberous sclerosis independent of mTOR. Neuron 84, 78–91.

Zheng, L., Michelson, Y., Freger, V., Avraham, Z., Venken, K.J., Bellen, H.J., Justice, M.J., and Wides, R. (2011). Drosophila Ten-m and filamin affect motor neuron growth cone guidance. PLoS ONE 6, e22956.

Zheng, X., Zhou, A.X., Rouhi, P., Uramoto, H., Borén, J., Cao, Y., Pereira, T., Akyürek, L.M., and Poellinger, L. (2014). Hypoxia-induced and calpain-dependent cleavage of filamin A regulates the hypoxic response. Proc. Natl. Acad. Sci. USA 111, 2560–2565.

Zhou, A.X., Hartwig, J.H., and Akyürek, L.M. (2010). Filamins in cell signaling, transcription and organ development. Trends Cell Biol. 20, 113–123.

Supplemental Information

The Oxygen Sensor PHD2 Controls Dendritic Spines

and Synapses via Modification of Filamin A

Inmaculada Segura, Christian Lange, Ellen Knevels, Anastasiya Moskalyuk, Rocco Pulizzi, Guy Eelen, Thibault Chaze, Cicerone Tudor, Cyril Boulegue, Matthew Holt, Dirk Daelemans, Mariette Matondo, Bart Ghesquière, Michele Giugliano, Carmen Ruiz de Almodovar, Mieke Dewerchin, and Peter Carmeliet
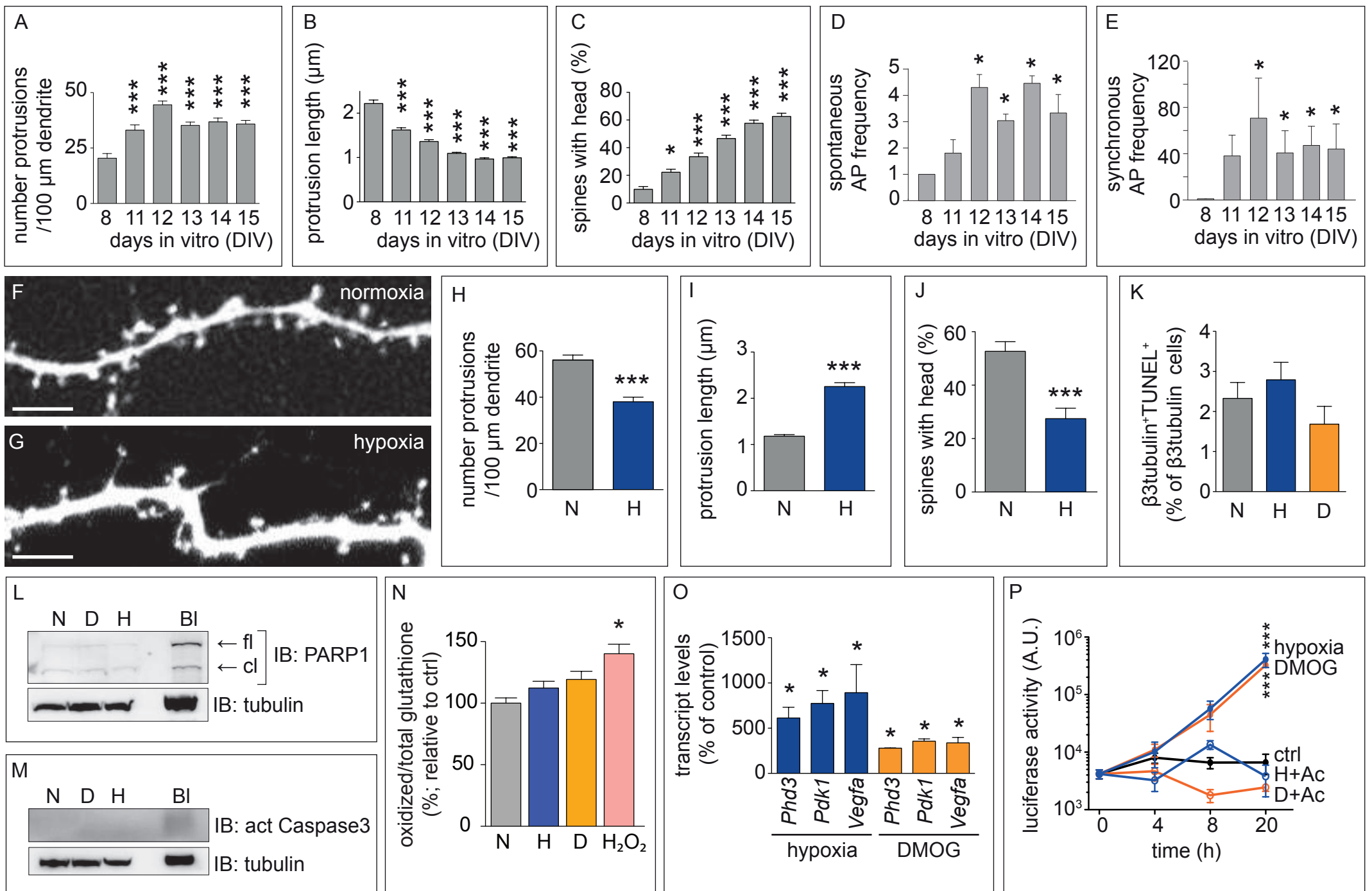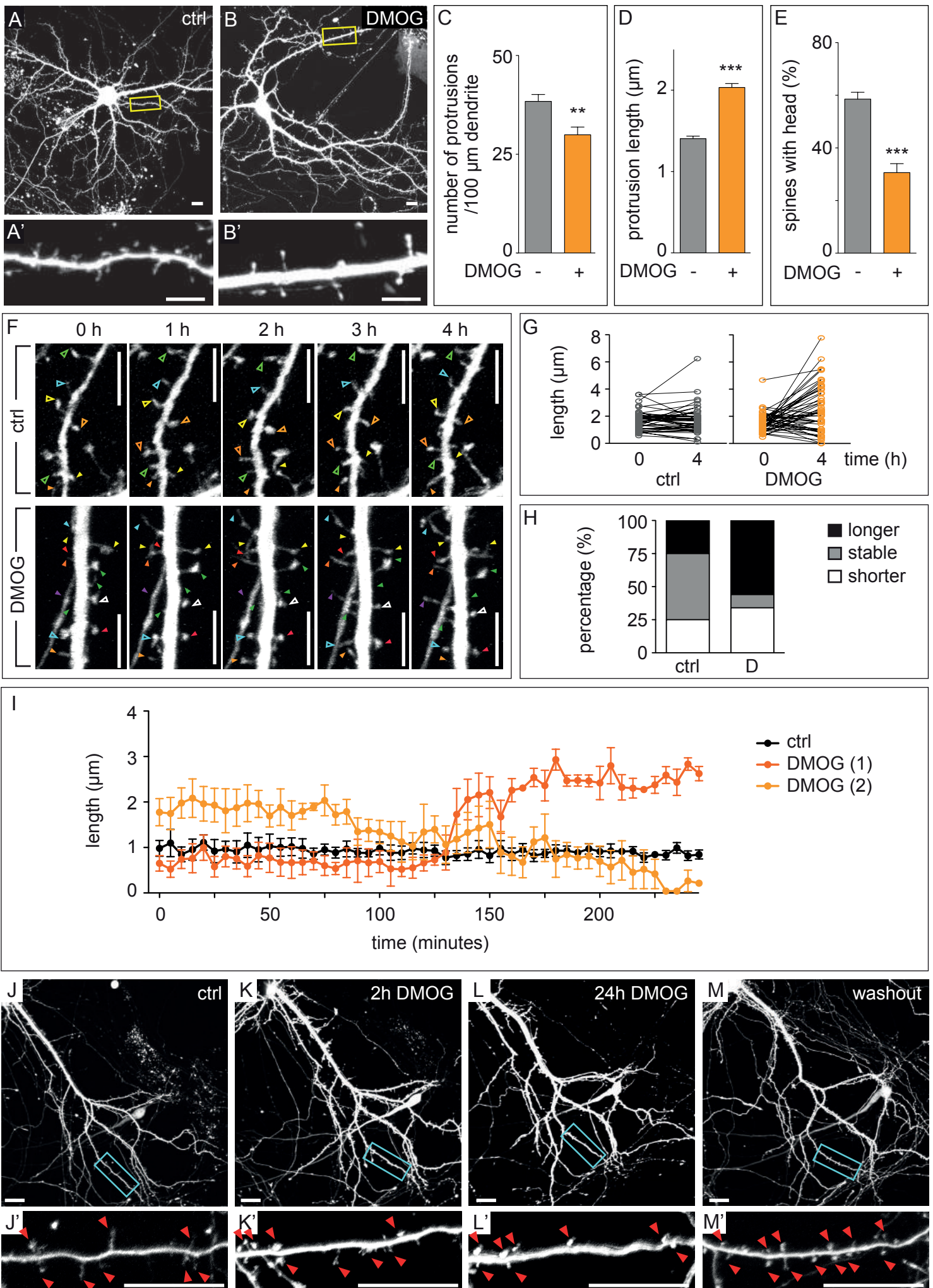
FIGURE S1

In all panels, N: normoxia, H: hypoxia (1% O_2), D: DMOG (250 μM). **A-C,** Time course analysis of dendritic spines in MHNs in vitro. Protrusion density (A), protrusion length (B), and percentage of spines with head (C) was evaluated in tdT labeled dendrites of MHNs at the indicated DIVs (n = 3 experiments, 30 neurons, 30-60 dendrites, 294-762 protrusions). **D,E,** Frequency of spontaneous action potential (AP) firing (D) and network-wide AP synchronization in vitro (E) at the indicated DIVs (n = 4 multi-electrode arrays (MEAs)). Data are normalized to the activity at 8 DIV. **F-J,** tdT-transfected 21 DIV MHNs in control (normoxia) conditions (F) or after 20 DIV in control conditions plus an additional 16 hr in hypoxia (G), and analyzed for protrusion density (H), protrusion length (I) and percentage of spines with head (J) (n ≥ 7 neurons, 12 dendrites, 350-500 protrusions). **K,** Quantification of apoptotic (TUNEL[+]) 14 DIV MHNs after control, hypoxia or DMOG treatment for 16 hr. **L,** Representative immunoblot (IB) for PARP1 and tubulin in lysates from 14 DIV MHN after control (normoxia), DMOG or hypoxia treatment for 16 hr. Brain lysate (Bl) was used as positive control. Arrows indicate full-length (fl) or cleaved (cl) PARP1. **M,** Representative IB for active (act) caspase3 and tubulin in lysates from 14 DIV MHN after control (normoxia), DMOG or hypoxia treatment for 16 hr. Brain lysate (Bl) was used as positive control. **N,** Content of oxidized glutathione (GSSG) vs. total glutathione (GSSG + GSH) (expressed in % of the value in normoxia) in 14 DIV MHNs in control normoxic conditions, hypoxia or DMOG treatment for 16 hr. MHNs treated with 100 μM H_2O_2 for 1 hr were used as a positive control (H_2O_2). **O,** RT-PCR expression analysis of hypoxia-responsive genes in MHNs exposed to hypoxia or treated with DMOG for 16 hr (expressed in % of normoxia control; n = 3 experiments). *Phd3*, prolyl hydroxylase domain 3; *Pdk1*, pyruvate dehydrogenase kinase 1; *Vegfa*, vascular endothelial growth factor A. **P,** Quantification of luciferase activity from MHNs transfected with the HIF-dependent luciferase reporter HRE::luc plasmid and incubated for the indicated time points in control (ctrl) conditions, DMOG (D) treatment or hypoxia (H) alone or combined with the HIF-inhibitor acriflavine (Ac). A.U., arbitrary units. Data are mean ± SEM. *p < 0.05, ***p < 0.001. Scale bar, 5 μm (F,G).

FIGURE S2

A-E, YFP-transfected MHNs were incubated for 16 hr under control (A) or 250 µM DMOG (B) and analyzed for protrusion density (C), protrusion length (D) and percentage of spines with head (E) (n = 3 experiments, ≥ 21 neurons, > 550 protrusions). A'-B' show higher magnifications of the box in A or B. **F**, Snap-shot images at the start (0) and after 1, 2, 3 or 4 hr of time-lapse recording of 14 DIV tdT-labeled MHNs, in control (upper) or DMOG conditions (lower). Solid arrowheads: spines with persistent increase or decrease in length; open arrowheads: spines that do not change their length. Each color denotes a distinct spine. **G,H**, Length of single protrusions at 0 and 4 hr recording for control and DMOG (G; n ≥ 40) and distribution of spines according to length variation (H). Stable: Δ-length ≤ 0.2 µm..**I,** Diagram showing the average length of randomly selected control (black) and DMOG-treated (orange) dendritic spines over time, showing different subpopulations responding to the treatment by reducing (light orange) or increasing (dark orange) their length; n = 5 spines per condition; representative of 3 experiments. **J-M',** Representative pictures of the same tdT transfected MHN taken at 13 DIV before treatment (J,J'), at 14 DIV after DMOG treatment for 2 hr (K,K'), at 15 DIV after DMOG treatment for 24 hr (L,L'), and at 18 DIV after washout for 3 DIV (M,M'). J'-M' show higher magnification of the boxed areas in J-M; red arrowheads: dendritic protrusions. Data are mean ± SEM. **p < 0.01, ***p < 0.001. Scale bar, 5 µm (A',B',F), 10 µm (A,B), 20 µm (J, J'-M, M').

FIGURE S3

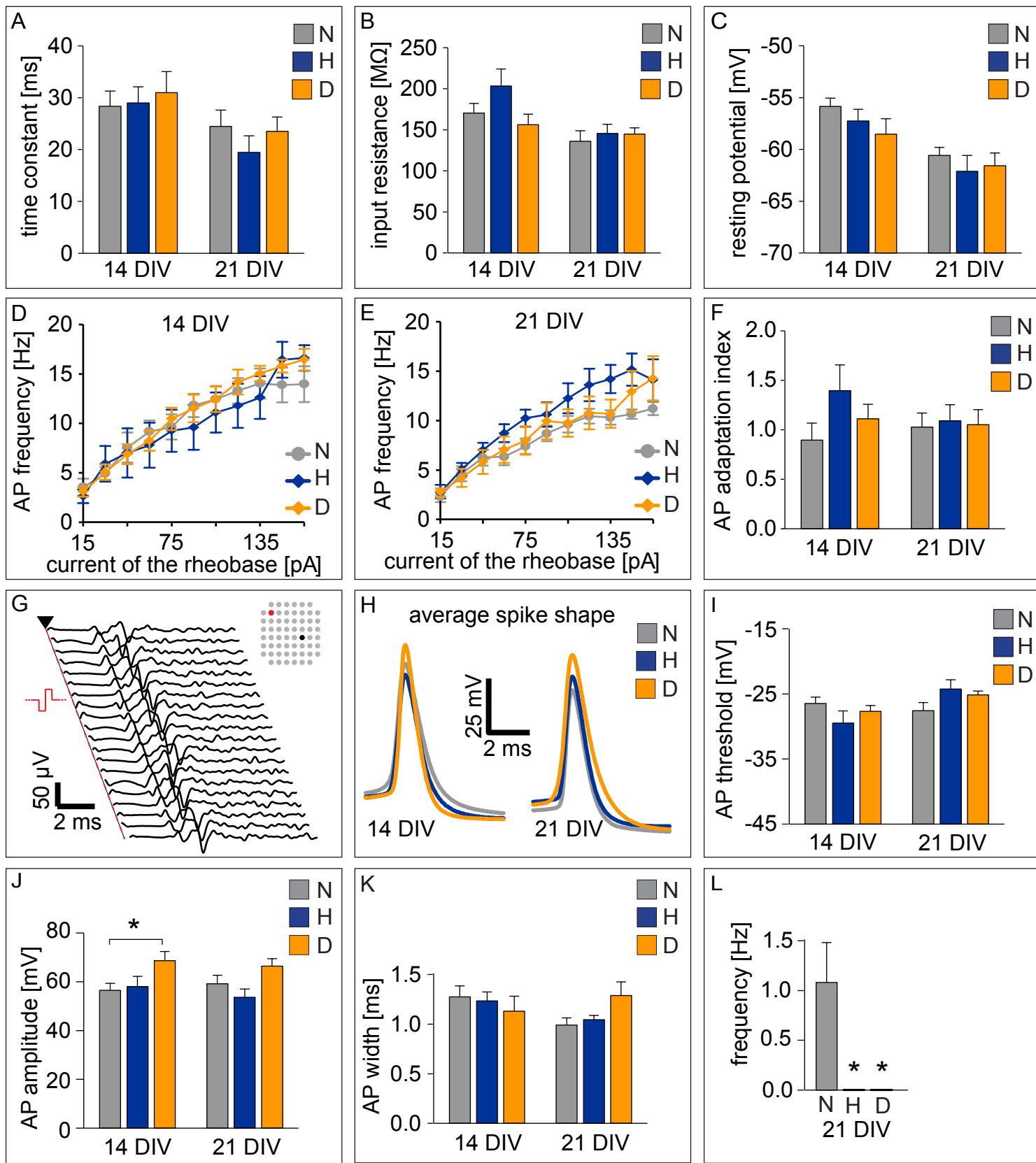In all panels, N: normoxia, H, hypoxia (1% O_2), D: DMOG (250 μM (A-F,H-L) or 1 mM (N,O)), H/N: hypoxia o/n followed by 24 hr normoxia. **A-C,** Single-neuron passive electrical properties of 14 and 21 DIV MHNs, measured by patch-clamp at the soma (n = 30 neurons) and quantification of the membrane time constant (A), apparent input resistance (B), and membrane resting potential (C). **D-F,** Excitable, active electrical neuronal properties (n = 30 neurons) of 14 (D,F) and 21 DIV (E,F) MHNs, studied by the relationship between current amplitude of the rheobase and the mean frequency of evoked action potential (AP; D,E), and by the temporal adaptation of successive APs in a train (F). **G,** Antidromic APs could be elicited with no failures during hypoxia by 20 repeated extracellular electrical pulses (monopolar configuration, biphasic waves, 1 ms x 800 mV, negative phase first) delivered via substrate-integrated multi-electrode arrays (MEAs). The inset sketches the MEA layout, with the stimulating microelectrode in red, and the recording microelectrode in black. The resulting traces were comparable to those obtained in normoxia (not shown) in their "all-or-none" quality, directly arising from the unaltered cellular and axonal excitability (see also panels D,E). **H**, Average spike shape of spontaneous APs, after recording non stop for 5 minutes and averaging all APs fired, in 14 or 21 DIV MHNs in the indicated conditions. **I-K**, Typical AP features of 14 and 21 DIV MHNs, including threshold (i.e., calculated as the first maximum of the third derivative of the membrane voltage during an AP; I), peak amplitude (J), and width (K). **L**, Spontaneous AP firing as recorded intracellularly by patch-clamp in 21 DIV MHNs, in the indicated conditions, shown as average frequency. **M**, Representative raster plots of the spiking activity, detected in the same neuronal culture by a MEA of 60 extracellular microelectrodes, in normoxia, during hypoxia (after overnight treatment), and 24 hr after return to normoxia. The spontaneous occurrence of one or more action potentials, detected at each of the 60 distinct microelectrode locations, is indicated by a black dot: prominent episodic synchronization is apparent from the vertical structures (i.e., bursts) in the plots and indirectly indicates functional glutamatergic synaptic transmission. **N,O**, Frequency of spontaneous AP firing (N) and spontaneous network-wide AP synchronization (O) (n = 4 MEAs/condition), for the indicated DIV and condition. **P-S,** MHN at 14 DIV transfected with YFP (green) and subjected at 20 DIV for 16 hr to normoxia (P), hypoxia (Q) or 250 μM DMOG (R), fixed and stained for presynaptic synaptophysin (red). The red dots lying outside of the YFP^+ neuron are from neighbouring neurons. Quantification of synaptic density per dendritic length (by counting the yellow clusters and the red clusters in immediate apposition with the dendrite/spine) is shown in S (n ≥ 10 neurons). Data are mean ± SEM. *p < 0.05, **p < 0.01, ***p < 0.001 (vs. normoxia ctrl).
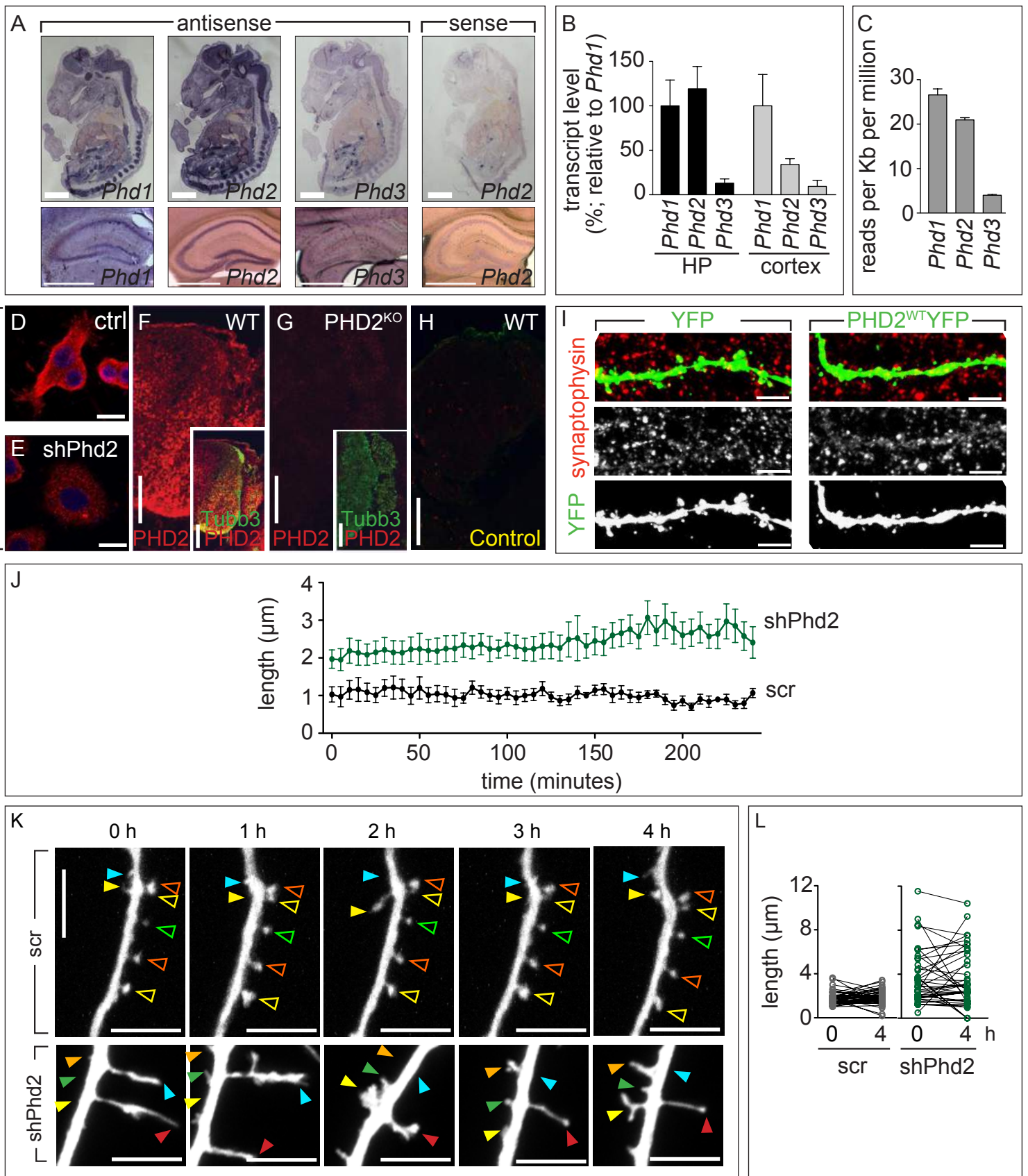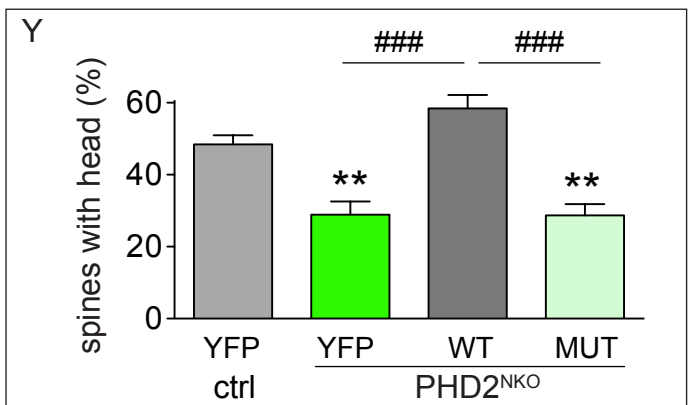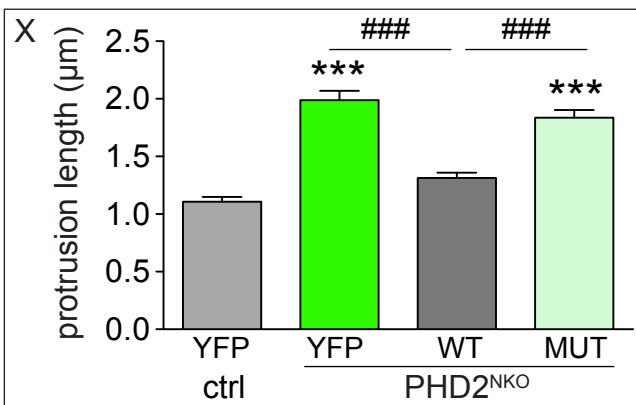
FIGURE S4
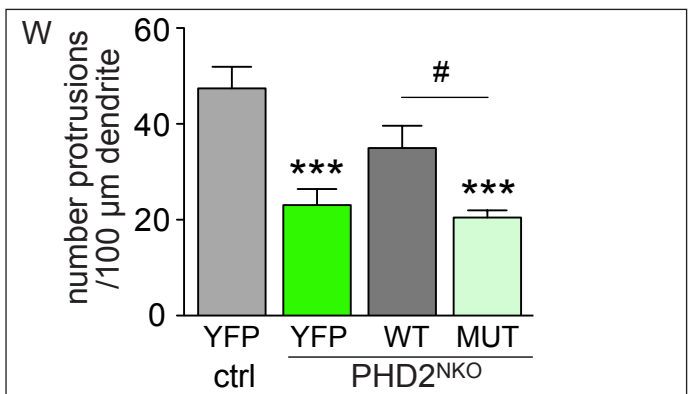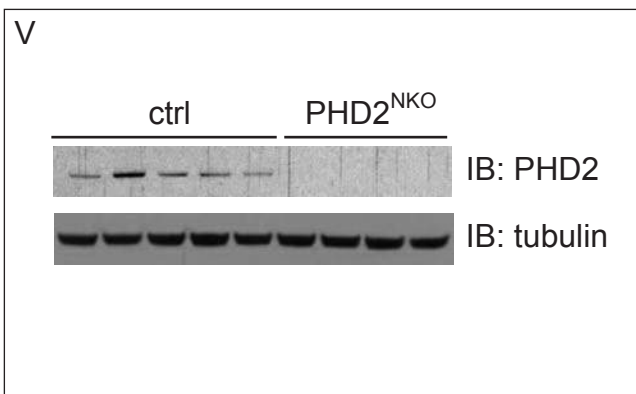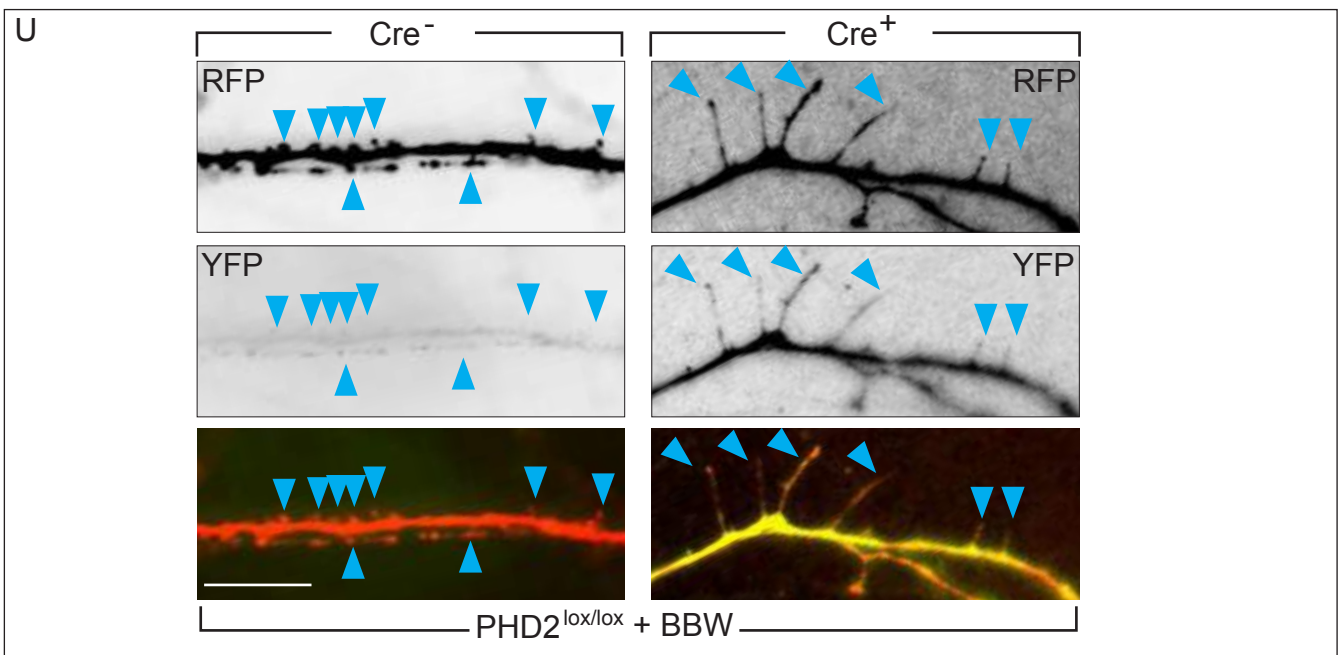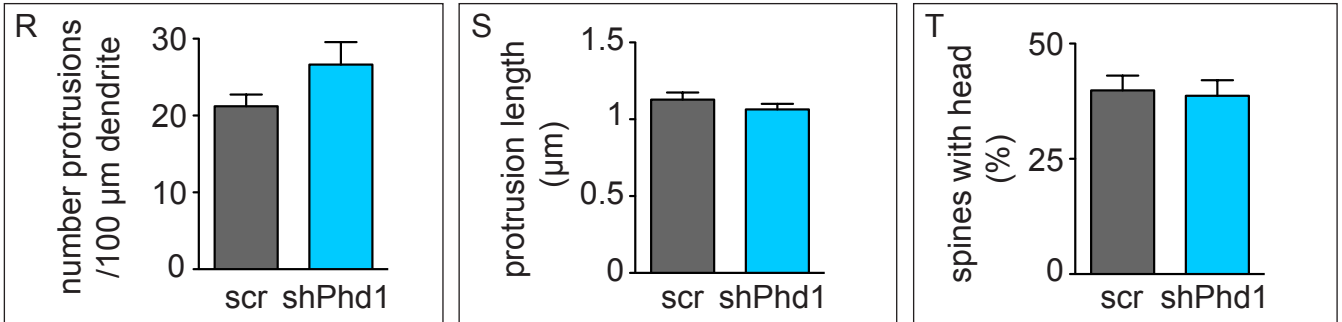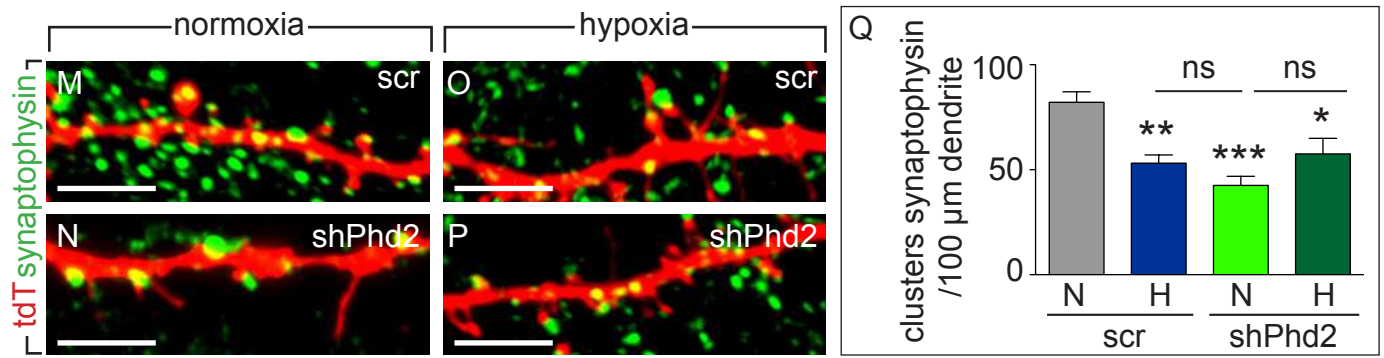
FIGURE S4 - continued

A, *In situ* hybridization with *Phd1 (also known as Egln2)*, *Phd2 (Egln1)* and *Phd3 (Egln3)* antisense probes or *Phd2* sense probe, in cryosections from E14.5 mouse embryos (upper panels) or in free-floating adult hippocampal coronal sections (lower panels). **B,** Relative mRNA expression of *Phd1*, *Phd2* and *Phd3* genes in E17 hippocampus (HP) and E14.5 cortex (n = 3 embryos). **C,** Quantitative mRNA expression of *Phd1*, *Phd2* and *Phd3* genes in 2 weeks old mouse brains by RNA-seq analysis (n = 3 mice). **D,E,** PC12 cells in control conditions (ctrl, D) or upon silencing of *Phd2* (shPhd2, E) and immunostained for PHD2 (red) and DAPI (blue), showing only negligible (background) staining upon *Phd2* silencing. **F-H,** Immunostaining for PHD2 (red) in cryosections from the trunk of E11.5 control (F) or PHD2^{KO} littermates (G). Small insets show co-staining with the neuronal marker ßIII-tubulin (Tubb3, green). Control staining without both primary antibodies (H). **I,** Representative images of MHNs transfected with YFP or PHD2^{WT}YFP expression constructs (green in top panels; white in lower panels) and immunostained for synaptophysin (red in top panels; grayscale in middle panels), showing the expression pattern of PHD2^{WT}YFP in neurons in culture, including its presence in postsynaptic sites. The red dots lying outside of the YFP$^+$ neuron are from neighbouring neurons. **J,** Diagram showing the average length of 5 representative scr (black) or shPhd2 (green) dendritic spines over time; representative of 3 experiments. **K,** Snap-shot images at the start (0) and after 1, 2, 3 or 4 hr of time-lapse recording in normoxia of 14 DIV MHNs co-transfected with YFP or EGFP plus scrambled control shRNA (scr, upper panels) or shPhd2 (lower panels),. Solid arrowheads: spines with persistent increase or decrease in length (longer or shorter at 4 hr, as compared to the start); open arrowheads: spines that do not change their length. Each color denotes a distinct spine. **L,** Length of single protrusions at 0 and 4 hr recording for control and *Phd2* silenced neurons; n ≥ 45 spines. **M-Q,** MHNs were co-transfected at 14 DIV with tdT (red) and with either scr (M,O) or shPhd2 (N,P), subjected at 20 DIV for 16 hr to normoxia (M,N) or hypoxia (1% O$_2$, O,P) and stained for synaptophysin (green). The green dots lying outside of the tdT$^+$ neuron are from neighbouring neurons. Quantification of synaptic density per dendritic length (yellow clusters and green clusters in immediate apposition with the dendrite/spine) is shown in panel Q (n = 8-14 neurons). **R-T,** Quantification of protrusion density (R), protrusion length (S) and percentage of spines with head (T) of MHNs transfected with scr or shPhd1 (n ≥ 10 neurons, 14-15 dendrites, >200 protrusions). **U,** MHNs isolated from *Phd2$^{lox/lox}$* E16.5 embryos were transfected with the Brainbow1.0 plasmid (BBW) alone (Cre$^-$) or combined with a Cre-recombinase expressing plasmid (Cre$^+$) at 7 DIV, and imaged at 14 DIV. Note that the Cre$^-$ MHN expresses only RFP, while the Cre$^+$ MHN expresses YFP and residual RFP. Arrowheads: dendritic protrusions. **V,** Representative IB for PHD2 and tubulin of homogenates obtained from the hippocampus of control (ctrl) and PHD2^{NKO} littermates. **W-Y,** Quantification of protrusion density (W), protrusion length (X) and percentage of spines with head (Y) of 14 DIV MHN isolated from ctrl or PHD2^{NKO} littermates upon transfection at 7 DIV with YFP, PHD2^{WT}YFP (WT) or PHD2^{MUT}YFP (MUT)). Corresponding representative images are shown in Fig. 3S (n = 7-15 neurons, 203-335 protrusions). Data are mean ± SEM; ns = not significant, *p < 0.05, **p < 0.01, ***p < 0.001 vs. scr control in normoxia (Q) or vs. ctr (W-Y); #p < 0.01, ###p < 0.001 between indicated bars. Scale bar: 10 µm (D,E), 5 µm (I,K,M-P,U), 100 µm (F-H), 2000 µm (A).
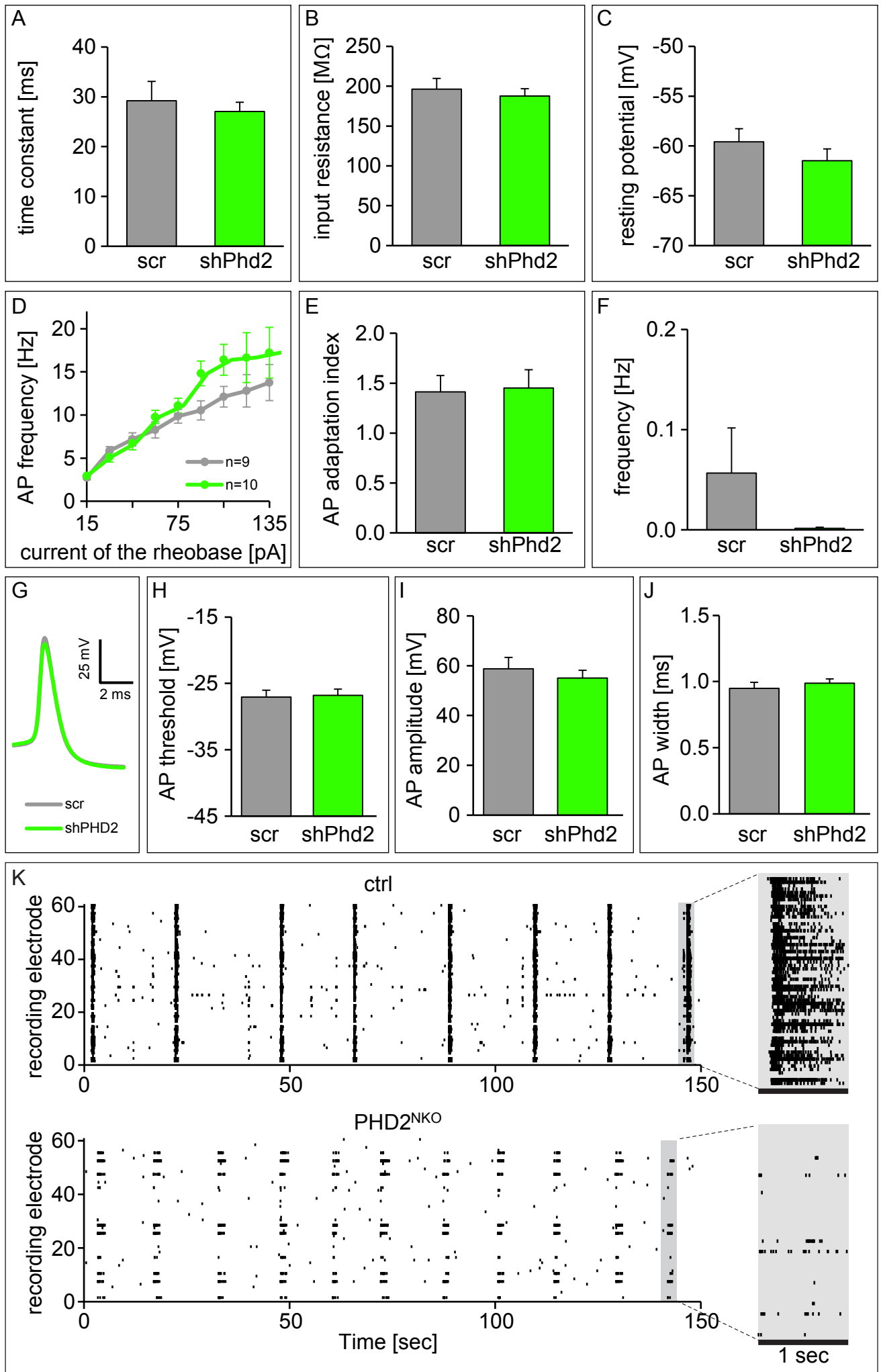
FIGURE S5

A-C, Single-cell passive membrane properties (membrane time constant (A), input resistance (B) and membrane resting potential (C)) measured from soma using patch-clamp recordings in MHNs transduced with lentiviral vectors expressing scrambled (scr) or shPhd2 (n = 27 neurons). **D,E,** Active electrical neuronal properties estimated by mean frequency of evoked action potential in response to current steps with increasing amplitude (D) and time adaptation of action potentials (E) in MHNs transduced with lentiviral vectors expressing scr or shPhd2 (n = 9-10 neurons). **F,** Network properties characterized by the frequency of spontaneous action potentials in MHNs transduced with lentiviral vectors expressing scr or shPhd2 (n = 9-10 neurons). **G-J,** Single action potential properties represented by average shape of action potentials (G), threshold (H), amplitude (I) and width (J), in MHNs transduced with lentiviral vectors expressing scr or shPhd2 (n = 9-10 neurons in H-J). **K**, Representative raster plots of the spiking activity at 14 DIV, detected in two multi-electrode arrays (MEAs) each obtained from a set of control (top) or PHD2^{NKO} neurons (bottom). The spontaneous occurrence of action potentials detected by each of the 60 distinct microelectrodes is indicated by a black dot. Prominent episodic synchronization is apparent in control but not in PHD2^{NKO} cultures. The insets highlight the differences in the firing of the two neuronal networks at higher temporal resolution. Data are mean ± SEM.
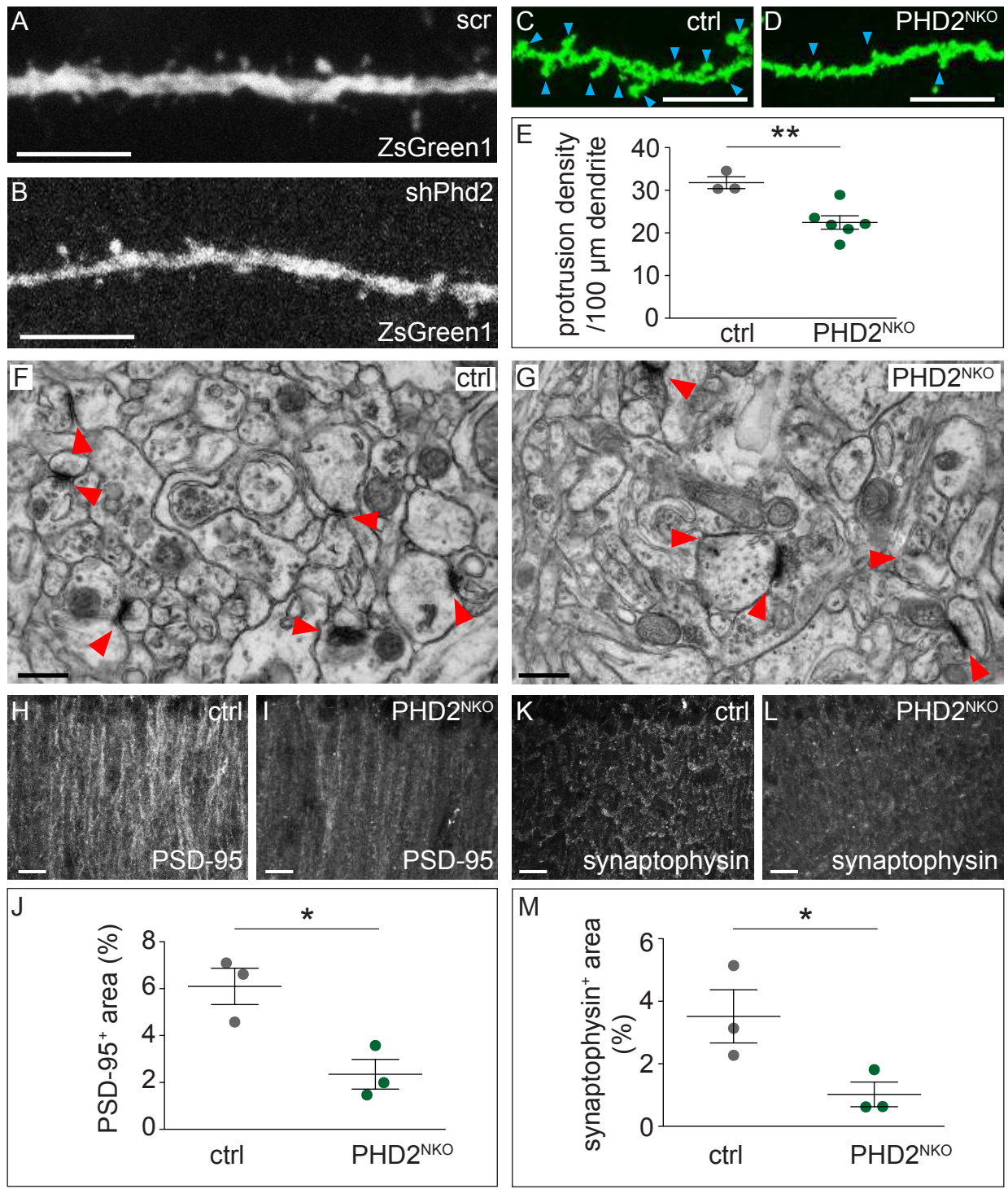
FIGURE S6

A,B, Representative ZsGreen1$^+$ dendritic segments from the CA1 region of hippocampal slices of 2-weeks old WT mice that were *in utero* electroporated at E15.5 with a scrambled control shRNA (scr) (A) or shPhd2 (B). **C-E,** Representative dendritic segments from hippocampi of 2 weeks old control (ctrl; C) or PHD2^{NKO} (D) mice, detected by using the Golgi impregnation imaged under the reflection mode of the microscope. Arrowheads: dendritic spines. Panel E shows the quantification of the dendritic protrusion density (n = 3-6 animals). **F,G,** Representative images of the *stratum radiatum* of the CA1 hippocampal region of ctrl (F) or PHD2^{NKO} (G) mice obtained by transmission electron microscopy. Red arrowheads: post-synaptic densities (n = 3-4 animals). **H-M,** Representative images of anti-PSD-95 staining (H,I) and anti-synaptophysin staining (K,L) of the *stratum radiatum* of the CA1 hippocampal region of control (ctrl; H,K) or PHD2^{NKO} (I,L) mice. Quantification of PSD-95$^+$ area (panel J; n = 3) and synaptophysin$^+$ area (panel M; n = 3) (after setting a common intensity threshold). Single data plus mean ± SEM are shown. *p < 0.05, **p < 0.01. Scale bar, 5 μm (A,B), 10 μm (C,D), 500 nm (F,G), 20 μm (H,I,.K,L).

A ctrl — FLNA
B shFlna — FLNA
C YFP FLNA
D YFP FLNA

E
| | tdT | FLNA^{CT}TQ2 | tdT FLNA^{CT}TQ2 |
normoxia
hypoxia

F ratio FLNA/drebrin (%) — H, NS, S, PSD — normoxia, hypoxia

G transcript level (% normoxia) — Vegfa**, Pfkfb3**, Slc2a1**

H ratio FLNA/tubulin (%) — normoxia 0 2 4 8, hypoxia 2* 4* 8* time (h)

I ratio FLNA/tubulin (%) — 0, 2, 2* +DMOG time (h)

J Flna mRNA expression (fold induction vs. t0) — ctrl, H, D

K ratio FLNA/tubulin (%) — normoxia: -, D*, MG*; hypoxia: -, Ac*, Cy*

L ratio FLNA/tubulin (%) — 0, 2, 2 2*, 2 5*, 2 10* time (h) MG132

M ratio FLNA/tubulin (%) — scr, shPhd2*, mycFLNA$^{D21-D23}$*

N ratio FLNA/drebrin (%) — ctrl, PHD2^{NKO} — H, NS, S, PSD

O ratio PSD-95/drebrin (%) — ctrl, PHD2^{NKO} — H, NS, S, PSD

P ratio synapt./drebrin (%) — ctrl, PHD2^{NKO} — H, NS, S, PSD

Q ratio syntaxin/drebrin (%) — ctrl, PHD2^{NKO} — H, NS, S, PSD

R ratio PTEN/drebrin (%) — ctrl, PHD2^{NKO} — H, NS, S, PSD

S ratio Calretinin/drebrin (%) — ctrl, PHD2^{NKO} — H, NS, S, PSD

FIGURE S7

A,B, PC12 cells in control conditions (ctrl, A) or after silencing of *Flna* (shFlna, B), and immunostained for FLNA (red). **C,D,** Representative images of YFP transfected RHNs immunostained for endogenous FLNA (red). Boxes denote regions that are shown at higher magnification in Fig. 4A. **E,** 14 DIV MHNs co-transfected with tdT (red) and C-terminus FLNA-TQ2 (FLNA^{CT}TQ2, green) incubated in normoxia (top) or hypoxia (bottom) for 16 hr. Left and middle panels: single tdT or FLNA^{CT}TQ2 signal channel, respectively, in gray scale. The right panels: merged images. **F,** Densitometric quantifications of the ratio of FLNA protein levels (normalized to drebrin) of the imm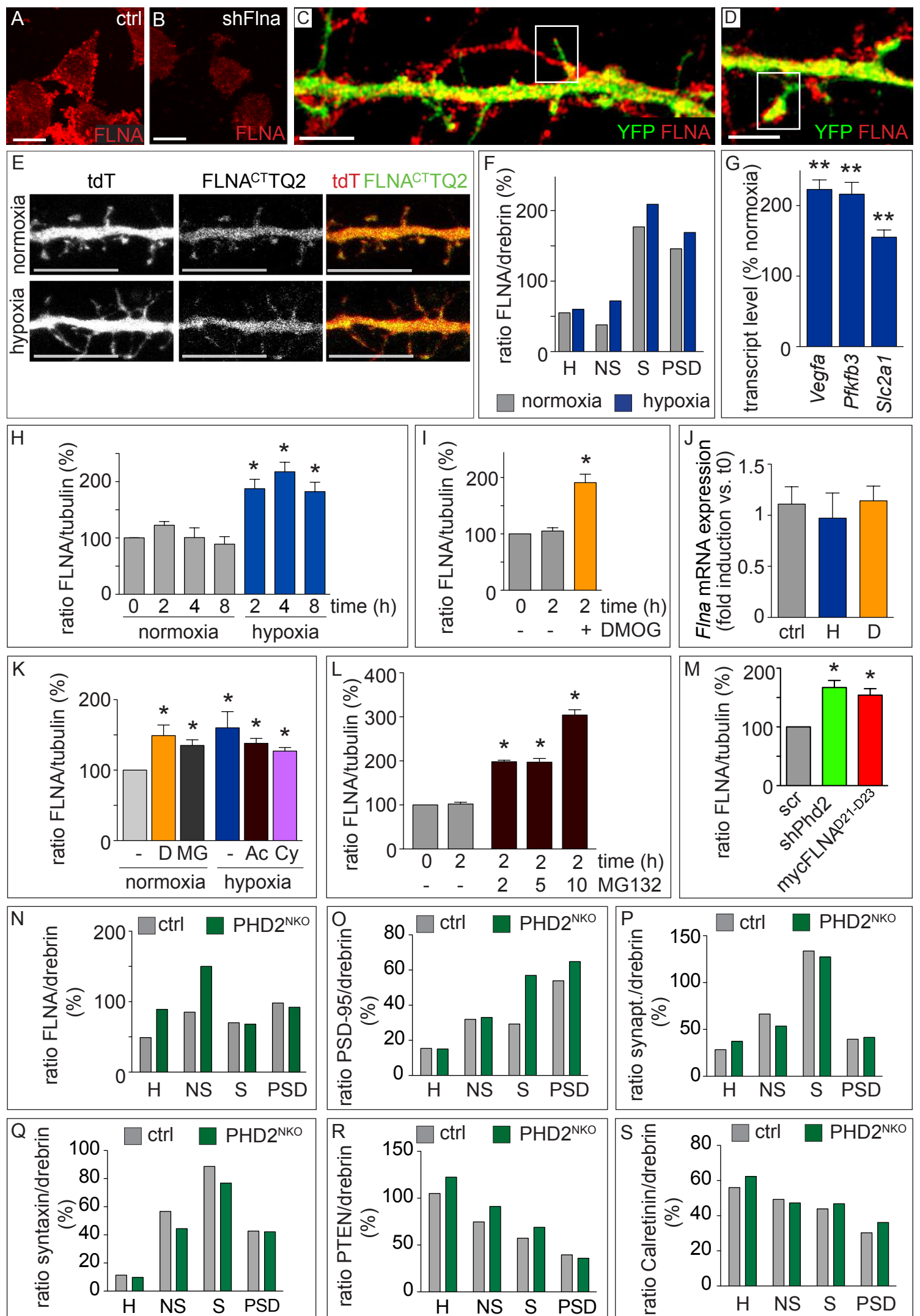unoblot (IB) shown in Fig. 4C. **G,** Quantification of mRNA transcripts of HIF-target genes. Two weeks old mice were maintained under normal atmospheric conditions or exposed to hypoxia (8% O_2) for 4-5 hr before sacrifice. mRNA was isolated from the brains and quantified by RNA-Seq (n = 3 mice). *Vegfa*, vascular endothelial growth factor A; *Pfkfb3*, phosphofructokinase-2/fructose-2,6-bisphosphatase 3; *Slc2a1*, solute carrier family 2 (facilitated glucose transporter) member 1 (Glut1). **H**, Densitometric quantification of FLNA IBs from 14 DIV MHNs incubated under hypoxia for the indicated time points (expressed in % of the value at 0 hr in normoxia, n = 5). A representative blot is shown in Fig. 4D. **I**, Densitometric quantification of FLNA IBs from 14 DIV MHNs treated for 2 hr without or with DMOG (n = 4). A representative blot is shown in Fig. 4E. **J,** Quantification of *Flna* transcript levels in MHNs under control (ctrl), hypoxia (H) or DMOG (D) treatment for 4 hr, normalized to the value at 0 hr (n = 3). **K**, Densitometric quantification of FLNA IBs from homogenates of MHNs in normoxia or hypoxia in the absence (-) or presence of DMOG (D), MG132 (MG), actinomycin D (Ac) or cycloheximide (Cy) (expressed in % of the value in untreated MHNs in normoxia, n = 3). A representative blot is shown in Fig. 4F. **L**, Densitometric quantification of FLNA IBs from homogenates of MHNs treated for 2 hr with increasing concentrations of MG132 (expressed in % of the value in untreated MHNs at 0 hr, n = 3). A representative blot is shown in Fig. 4G. **M**, Densitometric quantifications of FLNA IBs from homogenates of MHNs transduced with scr, shPhd2 or overexpressing myc-tagged FLNA deletion mutant D21-D23 (mycFLNA$^{D21-D23}$) (n = 3). A representative blot is shown in Fig. 4H. **N-S,** Densitometric quantifications of the levels of FLNA (N), the postsynaptic marker PSD-95 (O), the presynaptic markers synaptophysin (P) and syntaxin (Q) and of soluble fraction enriched markers PTEN (R) and calretinin (S) in mouse brain homogenate (H), non-synaptic fraction (NS), synaptic membranes (S) and PSD subfractions obtained from control (ctrl) or PHD2^{NKO} littermates, as shown in the IBs in Fig. 4I. Data are mean ± SEM. *p < 0.05, **p < 0.01. Scale bar, 10 μm (A,B,E), 2 μm (C,D).

A

IP: FLNA

NS syn

IB: FLNA

IB: PHD2 * ◄

B

mycFLNA: - CT D21-D23-WT H2-D24

IB: FLNA

IB: myc

* ◄ CT
◄ D21-D23
*
◄ H2-D24

IP: myc

C

-	-	+	-	+	PHD2^{MUT}YFP
-	+	-	+	-	PHD2^{WT}YFP
+	-	-	+	+	mycFLNA^{CT}

IP: myc

* ◄ IB: YFP (PHD2-YFP)

IB: myc (mycFLNA^{CT})

total lysates

IB: YFP (PHD2-YFP)

IB: myc (mycFLNA^{CT})

D

| ABD | 1 | 2 | 3 | 4 | 5 | 6 | 7 | 8 | 9 | 10 | 11 | 12 | 13 | 14 | 15 | H1 | 16 | 17 | 18 | 19 | 20 | 21 | 22 | 23 | H2 | 24 |

2250 efsiwtreagagglaiaveg**p**skaeisfedrkdgscgvayvvqe**p**gdyevsvkfneehi**p**ds**p**fvv**p**vas**p** 2320

2321 sgdarrltvsslqesglkvnq**p**asfavslngakgaidakvhs**p**sgaleecyvteidqdkyavrfi**p**rengvylidvkfngthi**p**gs**p**fkirvge**p** 2415

2416 ghggd**p**glvsaygagleggvtgn**p**aefvvntsnagagalsvtidg**p**skvkmdcqec**p**egyrvtyt**p**ma**p**gsylisikygg**p**yhiggs**p**fkakv 2508

E

glutath. PD

P2270 P2294 P2309 P2312 P2316 P2320   P2342 P2363 P2386 P2404 P2407

IB: YFP (PHD2^{MUT})

P2415 P2421 P2439 P2461 P2472 P2481   P2484 P2496 P2503

IB: YFP (PHD2^{MUT})

F

ratio OH-FLNA /total FLNA (%)

* *

| - | + | - | MG |
| - | - | + | Lact. |

G

2303_ F N E E H I P D S P F V V P V A S P S G D A R _2325

a unmodified

intensity

m/z

b OH-P2316

intensity

m/z

H

ratio OH-FLNA$^{D21-D23}$ /total FLNA$^{D21-D23}$ (%)

DMOG: - + - + - +

mycFLNA$^{D21-D23}$: WT P2309A P2316A
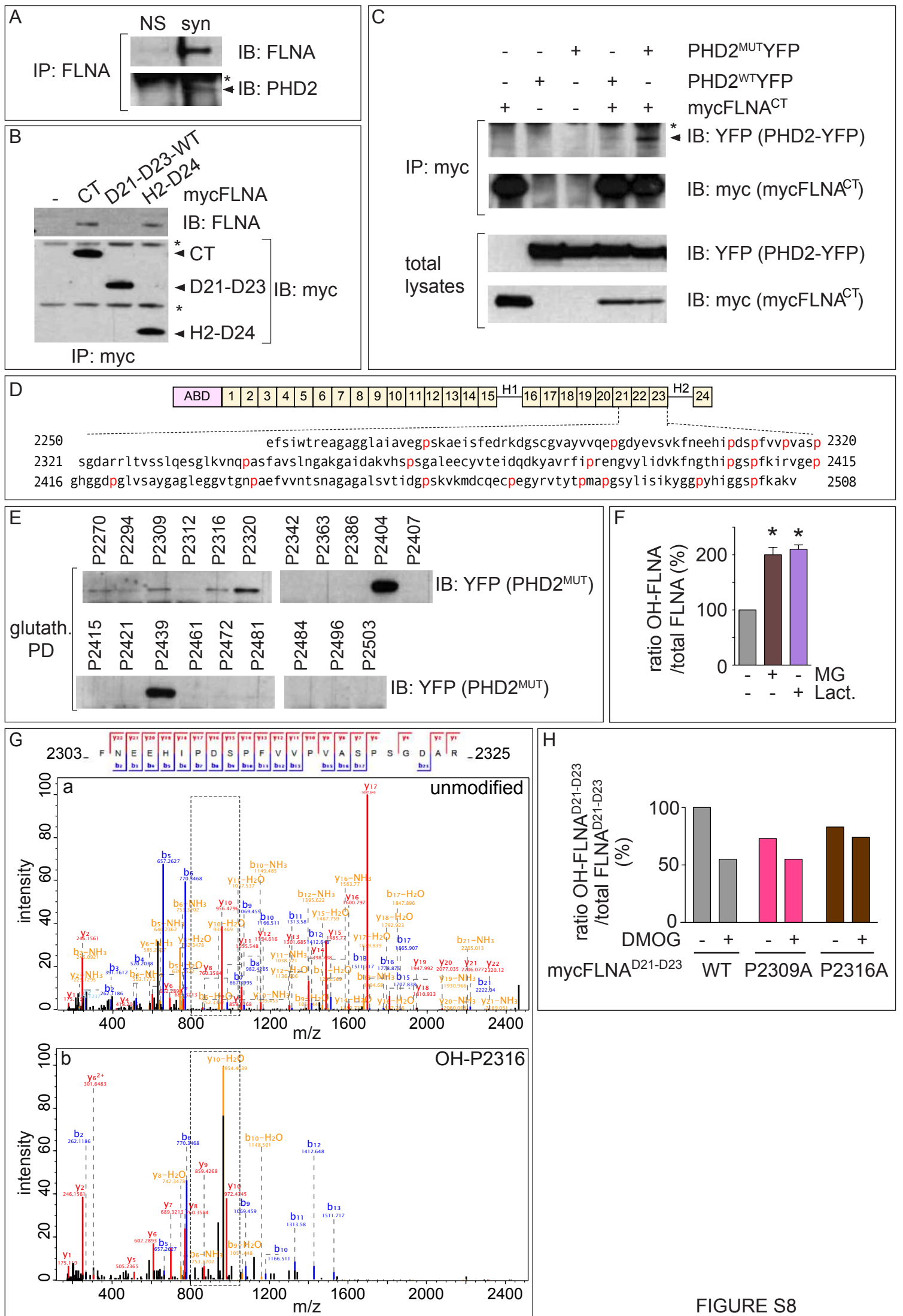
FIGURE S8

A, Representative IB for FLNA and PHD2 after immunoprecipitation (IP) of FLNA from non-synaptic (NS) and synaptic membrane (syn) subfractions of the brain of 2 weeks old mice. Arrow indicates PHD2, asterisk indicates the heavy chain of the IgGs used for the IP. **B,** Representative IB for myc and FLNA after IP of myc from HEK293T cells expressing myc-tagged FLNA deletion mutants mycFLNA^{CT} (CT), mycFLNA$^{D21-D23-WT}$ (D21-D23) or mycFLNA^{H2-D24} (H2-D24). Arrows indicate the myc-tagged deletion mutants; asterisks indicate the heavy and light chains of the IgGs used for the IP. **C,** Representative IB for myc and YFP after IP of myc from HEK293T cells expressing mycFLNA^{CT}, PHD2^{WT}YFP or PHD2^{MUT}YFP alone or a combination of them. Arrow indicates the PHD2 after the IP; asterisk indicates aspecific band. Total lysate controls are shown (bottom). **D,** Amino acid sequence of the D21-D23 deletion mutant of FLNA that interacts with PHD2. Each line corresponds to the sequence of the different domains. The proline residues are indicated in red. **E,** Recombinant GST-fusion peptides, each containing a proline residue in FLNA$^{D21-D23-WT}$ (flanked by 6 amino acids upstream and downstream of the respective proline residue), were incubated with homogenates of HEK293T cells expressing PHD2^{MUT}YFP. Glutathione-beads were used to pull-down the complexes, and bound PHD2^{MUT}YFP was identified by IB for YFP. **F,** Densitometric quantification of hydroxyl-FLNA level in HEK293T cells transfected with myc-FLNA and treated for 2 hr with MG132 (MG) or lactacystin (Lact.) (n = 3). A representative IB is shown in Fig. 5E. **G**, MS/MS fragmentation spectra of the unmodified (a) and hydroxylated P2316 (b; OH-P2316) sequence FNEEHIPDSPFVVPVASPSGDAR of FLNA. The boxed areas comprising the peaks corresponding to the proline P2316 containing fragments y10 are shown at larger scale in Fig. 5G. **H,** Densitometric quantification of the ratio hydroxylated/total mycFLNA$^{D21-D23}$ protein levels of IB from homogenates of HEK293T cells co-transfected with PHD2^{WT}YFP together with mycFLNA$^{D21-D23-WT}$, mycFLNA$^{D21-D23-P2309A}$ or mycFLNA$^{D21-D23-P2316A}$ in the absence or the presence of DMOG. The corresponding blot is shown in Fig. 5H. Data are mean ± SEM. *p < 0.05.
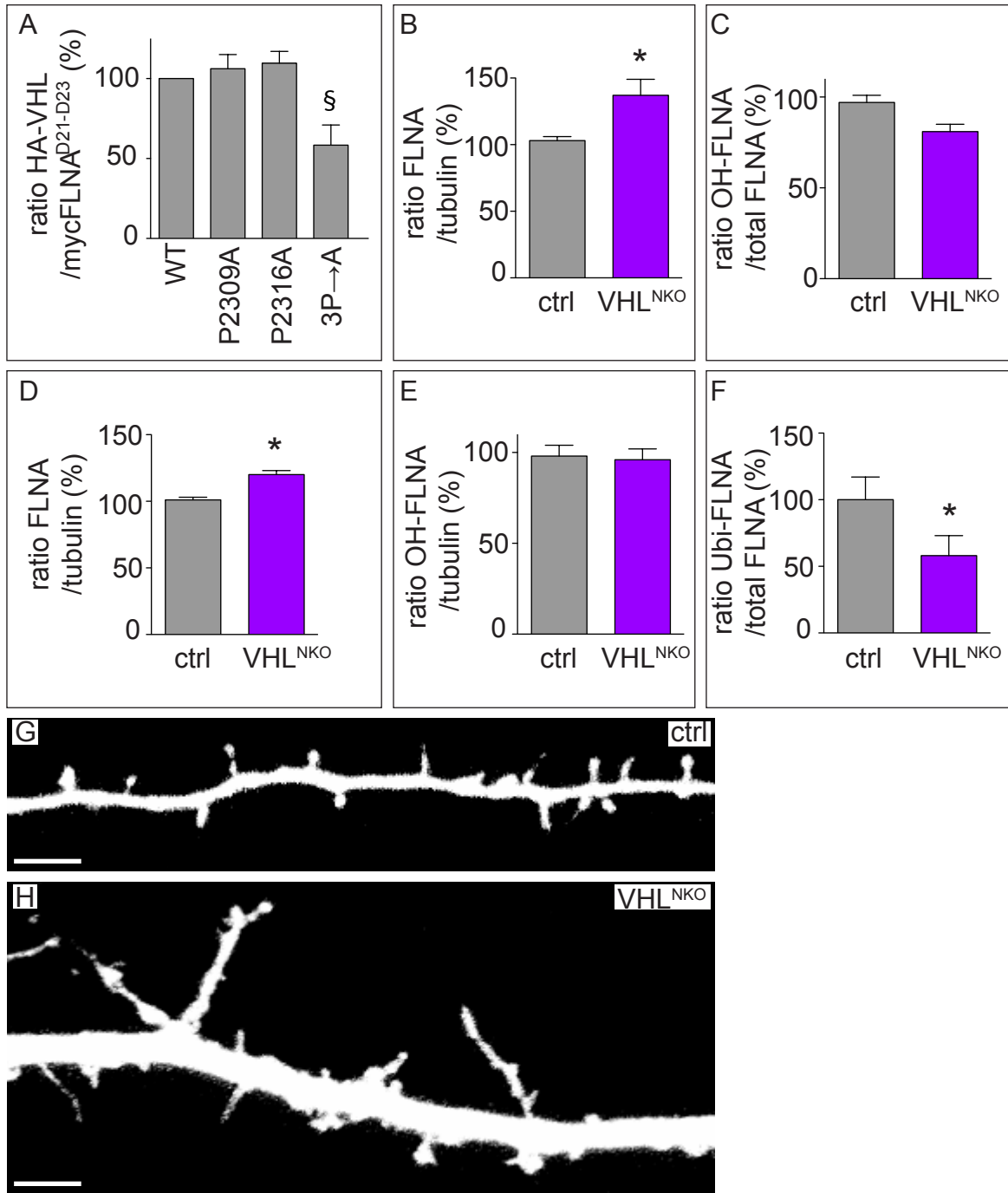
FIGURE S9

A, Densitometric quantification of the ratio of interaction between HA-VHL with wild type (WT) or mutant mycFLNA$^{D21-D23}$ (P2309A, P2316A or P2309/2312/2316A (3P→A)) (n = 3). A representative immunoblot (IB) is shown in Fig. 6C. **B**, Densitometric quantification of FLNA levels in brain homogenates obtained from E14.5 control (ctrl) or VHL^{NKO} littermates (n = 3-4 mice). The corresponding IB is shown in Fig. 6E. **C-E,** Densitometric quantification of the ratio of hydroxylated FLNA over total FLNA (C), FLNA protein level (D) or total hydroxyl-FLNA level (normalized to tubulin) (E) in brain homogenates obtained from E14.5 control (ctrl) or VHL^{NKO} littermates (n = 3-4 mice). The corresponding IB is shown in Fig. 6F. **F,** Densitometric quantification of the ubiquitinated-FLNA/total FLNA ratio in brain homogenates obtained from E14.5 control (ctrl) or VHL^{NKO} littermates and subjected to TUBE2 pull-down. The corresponding IB is shown in Fig. 6G (n = 2 mice). **G,H,** Representative images of 14 DIV MHNs from control (ctrl, G) or VHL^{NKO} (H) littermates and transfected with tdT. Data are mean ± SEM. * p < 0.05; § p = 0.07. Scale bar, 10 μm (G,H).

ANIMALS

Animal housing and experimental procedures were approved by the Animal Ethics Committee of the KU Leuven (Belgium). *Wild type* (WT) Swiss mice and Wistar rats were used. *Phd2$^{lox/lox}$* (Mazzone et al., 2009), PHD2-KO (Mazzone et al., 2009) and *Nestin*Cre (Tronche et al., 1999) mice had C57BL6 background. *Vhl$^{lox/lox}$* (Haase et al., 2001) and *Hif-1α$^{lox/lox}$* (Ryan et al., 2000) mice had BALB/c-C57BL6 mixed background.

MHN ISOLATION, CELL CULTURE, TRANSFECTION AND TRANSDUCTION

MOUSE AND RAT HIPPOCAMPAL NEURONS were isolated as previously described (Segura et al., 2007), and plated on coverslips or tissue culture plates coated with 0.2 mg/ml poly-D-lysine (Sigma) and 5 μg/ml laminin (Life Technologies). For the washout experiments, neurons were plated on culture plates marked with a grid (500 μm grid distance; IBIDI). Neurons were cultured in neurobasal medium supplemented with 1X B27 and 0.5 mM glutamine (all from Life Technologies). The neuronal density was 50-70,000 neurons per 24-well plate or 500,000 neurons per p35-dish (equivalent to 325-450 cells/mm^2). For in vitro electrophysiological experiments, cells were seeded on conventional glass coverslips or on substrate-integrated multi-electrode arrays at a density of 1,000 cells/mm^2 or 3,200 cells/mm^2, respectively. Neurons were grown for 7-14 days in vitro (DIV) and transfected with Lipofectamine2000 (Life Technologies) following the manufacturer's instructions, and analyzed at 14 or 21 DIV. When indicated, 3-5 DIV neurons were transduced overnight (o/n) using 10 MOI lentiviral particles. For adenoviral particles, isolated MHN were incubated with 10 MOI particles for 15 min before plating. *HUMAN EMBRYONIC KIDNEY (HEK) 293T CELLS* were maintained in Dulbecco Modified Earl Media (DMEM) supplemented with 10% fetal bovine serum (FBS), 2 mM glutamine, 100 U/ml penicillin and 10 μg/ml streptomycin (all from Life Technologies). HEK293T cells were transfected by the calcium phosphate precipitation method. When indicated, cells were treated with the following concentrations of compounds: 250 μM DMOG (Enzo Life Sciences), 10 μM MG132 (Calbiochem), 10 μM lactacystin (Millipore), 5 μM acriflavine (Sigma), 1 μg/ml actinomycin D (Sigma), 20 μg/ml cycloheximide (Sigma). *RAT PC12 CELLS* were maintained in DMEM supplemented with 5% FBS, 5% horse serum, 2 mM glutamine, 100 U/ml penicillin and 10 μg/ml streptomycin (all from Life Technologies). PC12 cells were transfected with siRNA sequences for either rat PHD2 or FLNA (IDT Trifect) by nucleofection, program U29 (AMAXA). Cells were routinely maintained in culture at 37ºC, 5% CO_2 and 21% O_2. Hypoxic incubations were made in a 94% N_2, 5% CO_2, 1% O_2 atmosphere for neurons, and 94.8% N_2, 5% CO_2, 0.2% O_2 for HEK293T cells.

MORPHOGENESIS OF DENDRITIC SPINES IN NORMOXIA

To characterize dendritic spines in vitro, we first monitored the maturation of dendritic spines in monocultures of mouse hippocampal neurons (MHNs) during 21 days in vitro (DIV). To visualize single dendritic protrusions, we transfected 6 DIV MHNs with yellow fluorescent protein (YFP), enhanced green fluorescent protein (EGFP) or tandem dimer tomato (tdT) fluorescent protein. At 8 DIV, MHNs extend few, long immature dendritic protrusions (Fig. S1A-C). Three days later, more numerous dendritic protrusions extended from dendrites (Fig. S1A) and progressively matured over time towards shorter mushroom-shaped spines at 15 DIV (Fig. S1A-C). Beyond 16 DIV, dendritic spine density and maturation were maintained (not shown).

To determine whether the morphological analysis of dendritic spine maturation correlated with neuronal activity, we used multi-electrode arrays (MEAs) to record the spontaneous action potentials (APs) fired by the neuronal network. These electrophysiological experiments revealed that the morphological maturation of the dendritic spines was accompanied by

increased synaptic activity. Indeed, over time and concomitant with morphological spine maturation, cultured MHNs acquired a spontaneous synchronized network-wide spiking activity that was evident after 12 DIV (Fig. S1A-E), as previously reported for ex vivo developing networks (Marom and Shahaf, 2002). Taken together, our morphological analysis and electrophysiology recordings, together with previous reports (Nwabuisi-Heath et al., 2012; Ziv and Smith, 1996), showed that dendritic spines of 14 DIV MHNs were undergoing progressive maturation.

SYNAPTOSOMAL FRACTIONATION

Post-synaptic density fractionations were prepared from brains obtained from 2 weeks old animals (mice or rats), as previously described (Cho et al., 1992), with inclusion of 10 μM of the proteasomal inhibitor MG132 in the lysis buffer.

PLASMIDS AND LENTIVIRAL VECTORS

The following plasmids were previously reported: pEYFP-N1 (Clontech), pcDNA3-myc-hFLNA-WT (Addgene #8982; transcript 1, UniProtID: Q60FE5 (Woo et al., 2004)), p-sh-SCR and p-shPHD2 (Leite de Oliveira et al., 2012; Mazzone et al., 2009), pRSET-B-tdTomato (Shaner et al., 2004), 9xHRE::Luciferase (Aragones et al., 2001), pBrainbow1.0 (Livet et al., 2007), pOG231-NLS-Cre (O'Gorman et al., 1991), HA-VHL-pRc/CMV (Addgene #19999 (Iliopoulos et al., 1995)), pCAGGS-GFP (Niwa et al., 1991) and pCAGGS-RFP-11 (Attardo et al., 2008). Murine $Phd2$ was cloned in frame in the pEYFP-N1 vector, to generate the PHD2^{WT}YFP fusion protein. The myc-tagged deletion mutants of hFLNA were generated by PCR from the pcDNA3-myc-hFLNA-WT plasmid. The TQ2-labeled full-length and C-terminus (2250-2639 aa.) of $hFLNA$ were cloned in frame in the pTQ2-N1 plasmid (Goedhart et al., 2012). The PHD2^{MUT}YFP mutants (H290A/D292A (Vogel et al., 2010), mycFLNA$^{D21-D23-P2309A}$, mycFLNA$^{D21-D23-P2316A}$ and mycFLNA$^{D21-D23-3P \rightarrow A}$ (P2309/2312/2316A) were generated using the QuickChange mutagenesis kit (Stratagene). GST-fusion proteins were made by cloning the coding sequence of the $FLNA$ fragments in the pGEX4-T2 plasmid (GE Healthcare). Lentiviral vectors were made using the pLVx-shRNA2 (scr, shPhd2, shPhd1, shFlna; Clontech), pLKO (scr, shVhl; Sigma) or pRRL (mycFLNA(D21-D23)) backbones.

LUCIFERASE ACTIVITY

Cells expressing Firefly luciferase were lysed and enzymatic luciferase activity was measured in a Microlumat LB96V Luminometer (Berthold Technologies).

IMMUNOBLOTS, IMMUNOPRECIPITATIONS AND PULL-DOWNS

For immunoblots, protein samples were separated by SDS-PAGE and transferred to 0.45-mm nitrocellulose membranes (Life Technologies). For immunoprecipitation, cells or tissue from mice or rats were lysed in chilled lysis buffer (50 mM Tris-HCl pH 7.5, 150 mM NaCl, 0.1% Triton-X100, 0.1% Brij35, 10% glycerol, 10 μM MG132 1% Complete protease inhibitor and 1% PhosSTOP (both from Roche)), and centrifuged at 15,000g for 10 min at 4ºC. Antibodies were pre-bound to protein A– or protein G–coated Dynabeads (Life Technologies) or agarose beads (Pierce or GE Healthcare). Lysates were incubated for 2 hr-o/n at 4ºC. To isolate ubiquitinated proteins, samples were lysed in cold lysis buffer containing 10 μM PR-619 (Sigma), and centrifuged at 15,000g for 10 min at 4ºC. Lysates were incubated with agarose-TUBE2 (Life Sensors) for 16 hr. In vitro binding assays were performed with GST-fusion proteins (expressed in $E. coli$ BL21-Gold (DE3; Life Technologies)) and cell homogenates obtained from HEK293T cells transfected with YFP or PHD2^{MUT}YFP, and incubated for 2 h at 4ºC. GST complexes were pulled-down with glutathione-coated beads (GE Healthcare). For antibodies used in immunoblots, see below.

RNA ANALYSIS

IN SITU HYBRIDIZATION: In situ hybridizations (ISH) were made as previously reported (Ruiz de Almodovar et al., 2011), using DIG-labeled antisense probes for murine *Phd1 (Egln2)*, *Phd2 (Egln1)* or *Phd3 (Egln3)* or sense probes as control on PFA fixed cryosections or free-floating vibratome sections. *RT-PCR:* Cells were lysed and total RNA was isolated using the PureLink RNA Mini Kit (Life Technologies). Complementary DNA was synthetized by the QuantiTect Retrotranscriptase reaction (Qiagen). RNA expression analysis was performed by Taqman quantitative RT-PCR using in house-designed primers and probes or premade primer sets (IDT). Sequences or ID numbers are available upon request. *RNA-SEQ*: Brains of 2 weeks old mice were collected and total RNA was isolated using TRIZOL (Life technologies). Quantitative RNA-seq analysis (Illumina) was performed by the Genomics Core (KU Leuven-UZ Leuven).

IMMUNOHISTOCHEMISTRY

Immunohistochemical stainings were performed on 4% PFA fixed MHN or thick free-floating brain cryosections. Samples were permeabilized with PBS-0.1% Triton X-100, and blocked with 10% goat serum. Primary antibodies (see below) were incubated o/n at 4ºC. Secondary antibodies were Alexa-488, -568 -633 or -647 conjugated antibodies (Life Technologies). Slides were mounted with ProLong-Gold anti-fade mounting media containing DAPI (Life Technologies). Analysis of spines in vivo was made in 80-100 μm vibratome sections. Golgi staining was performed in 2 weeks old littermates, using the FD Rapid Golgi Stain Kit (FD NeuroTechnologies). TUNEL staining was performed in 4% PFA fixed MHN using the *In Situ* Cell Death Detection Kit (Roche).

ANTIBODIES

The following antibodies were used: rabbit anti-PHD2 (Novus); mouse anti-myc (9E10) and rabbit anti-FLNA (for IHC of rat FLNA) (Santa Cruz); rabbit anti-FLNA (for mouse FLNA in IB), rabbit anti-hydroxyprolines, rabbit anti-PSD-95 and rabbit anti-drebrin (Abcam); mouse anti-FLNA (for IP of rat FLNA), mouse anti-PSD-95 and guinea pig anti-vGlut1 (Millipore); mouse anti-GFP (JL8, Clontech); rabbit anti-GFP (Fitzgerald); mouse anti-α-tubulin and rabbit anti-syntaxin (Sigma); rabbit anti-β-actin, rabbit anti-cleaved caspase 3, rabbit anti-pVHL and rabbit anti-PTEN (Cell Signaling); mouse anti-synaptophysin and rabbit anti-ubiquitin (Dako); rat anti-HA (Roche); goat anti-HIF-1α (R&D Systems); rabbit anti-PARP1 (Enzo); rabbit anti-calretinin (Swant Inc.).

MASS SPECTROMETRY

IN GEL PROTEIN DIGESTION: Stained protein bands were excised from the gel, and in-gel tryptic digestion was performed as described previously (Wilm et al., 1996) with minor modifications. Briefly, after several washing steps (50 mM NH_4HCO_3/ 50% acetonitrile (ACN)) to eliminate the stain, the protein were reduced (10 mM DTT in 50 mM NH_4HCO_3 for 30 min at 56°C) and then alkylated (55 mM iodoacetamide in 50 mM NH_4HCO_3 for 30 min at room temperature in the dark). The gel pieces were washed in 50 mM NH_4HCO_3 and then dried in 100% ACN to be rehydrated in a sufficient covering volume of Trypsin solution (10 ng/μl in 10 mM NH_4HCO_3; Promega). Trypsin digestions were performed o/n at 37°C with shaking. Peptides were extracted once with 50 mM NH_4HCO_3, twice 5 % formic acid (FA) in 50% ACN and once with 100% ACN. The five extractions were combined and the mixture was dried down in a vacuum concentrator and then reconstituted in 12 μl H_2O/ACN/FA (98:2:0.1). *MASS SPECTROMETRY ANALYSIS, DATABASE SEARCH, AND PROTEIN IDENTIFICATION:* Digested peptides were analyzed by nano LC-MS/MS using an EASY-nLC 1000 (Thermo Fisher Scientific) coupled to a Q Exactive Orbitrap mass spectrometer. 5 μl of each sample were picked up at 300 nl/min, loaded on a home-made C_{18} 18 cm capillary column picotip silica emitter tip (75 μm diameter filled with 1.9 μm Reprosil-Pur Basic C_{18}-HD resin (Dr. Maisch GmbH, Ammerbuch-Entringen, Germany)) equilibrated in solvent A (0.1 % FA). The peptides were eluted using a 2 to 50 % two

slopes gradient of solvent B (0.1 % FA in ACN) during 47 min at 250 nl/min flow rate (total length of the chromatographic run was 80 min). The Q Exactive (Thermo Fisher Scientific) was operated in data-dependent acquisition mode with the XCalibur software (Thermo Fisher Scientific). Survey scan MS were acquired in the Orbitrap on the $300 - 1800$ m/z range with the resolution set to a value of 70,000 at $m/z = 400$ in profile mode (AGC target at 1^E6). The 15 most intense ions per survey scan were selected for HCD fragmentation (NCE 28), and the resulting fragments were analyzed in the Orbitrap at 35,000 of resolution (m/z 400). Isolation of parent ion was set at 2.5 m/z and Underfill ratio at 2.5%. Dynamic exclusion was employed within 30 s. Data were searched using MaxQuant (1.4.1.2 version) (with the Andromeda search engine) against the human database from SwissProt and TrEMBL (Jan 21st 2014, 88,500 entries, of which 39,715 from SwissProt). The following search parameters were applied: Carbamidomethylation of cysteines was set as a fixed modification, and oxidation of methionine, protein N-terminal acetylation and Oxidation of Proline were set as variable modifications. The mass tolerances in MS and MS/MS were set to 10 ppm for each, respectively. Maximum peptide charge was set to 7 and 5 amino acids were required as minimum peptide length. Peptides and proteins identified with an FDR lower than 0.1% were considered as valid identification. For GSSG/GSH MEASUREMENT, lysates from 14 DIV control or treated MHNs were collected and the level of GSSG in percent of GSSG + GSH was determined using liquid chromatography-mass spectrometry. As positive control, MHN were treated with 100 μM H_2O_2 for 1 hr.

IN-UTERO ELECTROPORATION

Pregnant mice were isofluorane anaesthetized at E15.5 and laparotomy was performed to expose the uteri. Circa 2 μl of PBS containing 5 mg/ml of plasmid was injected into the lumen of the embryonic forebrain followed by electroporation of the hippocampal anlage using 8 pulses of 40 V, 50 ms each at 1 s interval delivered through platinum electrodes using a BTX-830 electroporator (Genetronics) as previously described (Pacary et al., 2012). Dendritic morphology of hippocampal CA1 neurons was investigated at P15. Briefly, mice were intracardially perfused with 4% PFA, and brains were removed and post-fixed for additional 24 h in 4% PFA. Brains were dissected and post-fixed in the same solution overnight at 4°C. Coronal brain sections (100 μm thick) were cut on a vibratome and mounted with Prolong antifade mounting media (Life Technologies) and imaged.

IMAGING AND TIME-LAPSE RECORDINGS

IMAGING was performed using a Zeiss LSM 510 Meta NLO, Zeiss LSM 780 confocal microscope (oil immersion objectives EC Plan-Neofluar 40x with NA 1.3, Plan-Apochromat 63x with NA 1.4, and alpha Plan-Apochromat 100x with NA 1.46) (Carl Zeiss) or Leica SP8x confocal microscope (Leica) (oil immersion objective 63x with NA 1.4). Bright field images were acquired with an Axioplan-2 microscope coupled to an Axiocam HRc (Carl Zeiss). For TIME-LAPSE IMAGING UNDER NORMOXIA, pictures were acquired every 5 min for 4 h at 37°C using a Zeiss LSM 780 confocal microscope. In the case of DMOG treatment, the movie started just when the drug was added on the culture media. For TIME-LAPSE UNDER HYPOXIA, cells were under 0.5% O_2, 5% CO_2 and 37°C (GM230 Tri-Gas Mixer, CellASIC ® Onix Microfluidic Platform, Millipore) and images were captured every 5 min for 4 h at 37°C using a Zeiss LSM 510 Meta NLO. The movie just started when switching the cultures to hypoxic conditions. SUPER-RESOLUTION IMAGING was performed using a Zeiss Elyra Structured Illumination microscope (SR-SIM) (Carl Zeiss) equipped with an oil 63x Plan-Apochromat objective with NA 1.4, three SIM grid rotations and averaging 4 scans of each pixel. FLIM-FRET: Time-domain fluorescence lifetime imaging microscopy (FLIM) was performed in transiently transfected HEK293T cells grown on glass-bottom dishes and transfected with the indicated plasmids. FLIM data were obtained using a confocal laser-scanning Leica TCS SP5 microscope. A pulsed two-photon Titanium:sapphire laser (Mai Tai HP, Spectra Physics, Newport) tuned at 820 nm was used for excitation. The excitation light was directed to the sample through a 63x (NA 1.2) water immersion objective. The emission light was filtered using a short pass 665 nm filter and a BP480/40 nm band pass filter. Finally, an APD detector (H7429-40,

Hamamatsu) connected to PicoQuant TCSPC hardware (PicoQuant) was used to detect the emission light, allowing for time-correlated single photon counting. FLIM images were processed using SymPhoTime software (PicoQuant). The quality of the fit was judged by the reduced χ^2–values. For the majority of the pixels the reduced χ^2–value was smaller than 1.2. *GOLGI IMPREGNATION:* To detect the Golgi impregnation, the Zeiss LSM780 confocal microscope was automatically set up in reflection mode by using a 488 nm wavelength and replacing the dichroic filter by a 20/80 beam splitter (Spiga et al., 2011). Images were acquired with an alpha Plan-Apochromat 100x/1.46 oil objective. No barrier filter was used to direct the reflected light by the sample to the detector. *ELECTRON MICROSCOPY* was performed using a JEM-1400 transmission electron microscope (Jeol, Zaventem, Belgium), equipped with an 11Mpixel Olympus SIS Quemesa camera. Ctrl and PHD2^{NKO} littermates were processed as previously described (Arranz et al., 2015). Briefly, mice (n=3-4 mice) were transcardially perfused with 2.5% glutaraldehyde, 2% paraformaldehyde in 0.1 M cacodylate buffer. Brains were dissected and post-fixed in the same solution overnight at 4°C. Coronal brain sections (300 µm thick) were cut on a vibratome and rectangular pieces of tissue comprising the *striatum* were dissected. Tissue was post-fixed with 1% OsO_4, 1.5% $K_4Fe(CN)_6$ in 0.1 M cacodylate buffer, rinsed, stained with 3% uranyl acetate and dehydrated in graded ethanols and propyleneoxide, followed by embedding in EMbed812. Ultrathin sections (70nm) were obtained using an ultramicrotome (Leica Reichert Jung Ultracut E), mounted on 400 mesh copper grids and contrasted with uranyl acetate and lead citrate before being imaged. Images were taken at 2500X magnification.

MORPHOMETRIC ANALYSIS AND QUANTIFICATIONS

MORPHOMETRIC ANALYSIS AND QUANTIFICATIONS were done in primary and secondary dendrites, and the protrusions included in these dendrites. Synaptic density was assessed as previously described (Segura et al., 2007). Quantifications were done with NIH ImageJ software, using neurons from 3 independent experiments (isolations), with n $\geq$ 7 neurons per condition/experiment, unless otherwise stated. All quantifications and manual counting were performed by persons, blinded for the experimental conditions. *QUANTIFICATION OF PROTRUSION LENGTH IN TIME-LAPSE MOVIES* was determined as follows. We measured the length of the spines, at the starting point and after different time points. Spines with variations ≤0.2 µm were considered stable. All imaged spines were measured at the starting point (0 hr) and end (1 hr for hypoxia or 4 hr for DMOG and shPhd2) of the time-lapse imaging (Fig. 1G,O; Fig. 3O). For the quantifications monitored over time at different time intervals using control or DMOG-treated neurons (Fig. S2A), we selected spines that were ≤2 µm long at the start of the analysis (≈75-80% of the spines were ≤2 µm in both cases), since this is the length of mature spines in the hippocampus (Sorra and Harris, 2000). We then followed over time how these spines responded to control vehicle or DMOG treatment. To evaluate the effect of PHD2 silencing, MHNs were transfected at 7 DIV with scr or shPhd2 constructs, and evaluated at 7 days later. Spines showed differences in length (spines >2 µm: ≈25% for scr vs. ≈70% for shPHD2), and they were randomly selected for quantification (Fig. S3K). *SYNAPTIC DENSITY IN VIVO* was determined by transmission electron microscopy or by measuring the PSD-95$^+$ or synaptophysin$^+$ fluorescent signal detected per area unit of the stratum radiatum of the CA1 hippocampal region. For the latter analysis, the same threshold was set for all the images. *QUANTIFICATION OF SYNAPTIC DENSITY IN VITRO* was determined as previously reported (Hotulainen et al., 2009; Kayser et al., 2008; Segura et al., 2007). Briefly, to identify single dendrites, we transfected MHN at 14 DIV either with YFP (green) or tdTomato (tdT; red) fluorescent proteins, and performed the staining at 21 DIV. We performed two different stainings: (I) anti-vGlut and anti-PSD-95 co-staining or (II) anti-synaptophysin staining. In the first case, we counted the number of vGlut$^+$/PSD-95$^+$ co-clusters that were localized on the fluorescently labeled dendrite. In the second case, for every single dendrite analyzed, we counted only those synaptophysin-positive clusters, (i) in which immunoreactive signal completely colocalized with the positive signal of the dendrite to yield a yellow cluster, or (ii) in which the immunoreactive signal was in immediate close apposition with ("touching") the positive signal of a dendrite or its spines, when analyzed with a 63-fold magnification. Under those conditions, the distance between the "touching" (red or green) signals was <200nm. *GENERAL NOTE:* In all panels showing immunostaining of neuronal cultures for vGlut1, synaptophysin, PSD95,

PHD2 or FLNA, immunoreactive signals are not only confined to the contours of the neuron under investigation (transfected with a fluorescent reporter to reveal its dendritic protrusions), but are also detectable as positive stainings in neighbouring neurons, which themselves are however not transfected with a fluorescent reporter and therefore their cell body is not visible in the image. High-density cultures had to be used to allow maintenance of the neuronal cultures for prolonged periods; transfection with fluorescent reporters (see above) was done using conditions transfecting only a fraction of the neurons to allow visualization of single neurons.

CELLULAR AND NETWORK ELECTROPHYSIOLOGY

Patch-clamp recordings of the membrane electrical potential of cultured hippocampal neurons were performed at 14 and 21 days after plating, as described (Reinartz et al., 2014) from the cell somata, under the whole-cell configuration using an Axon Multiclamp 700B Amplifier (Molecular Devices LLC, Sunnyvale, CA, USA), in current-clamp mode. Overnight hypoxic treatment or incubations with DMOG (250 μM) were performed the day prior the recordings. Patch electrodes were pulled from standard borosilicate glass (1B150F-4, World Precision Instruments, Sarasota, FL, USA) by a horizontal puller (P97, Sutter, Novato, CA, USA) to a resistance of 6-7MΩ. Electrodes were filled with an intracellular solution containing (in mM): 135 K-gluconate, 10 KCl, 10 HEPES, 0.2 EGTA, 4 Mg-ATP, 0.4 Na_3GTP, and 14 Na_2-phosphocreatine (pH 7.3, titrated with KOH). All recordings were obtained at 34°C shortly after replacing the culture medium by an artificial cerebro-spinal fluid, constantly perfused at a rate of 1ml/min and containing (in mM): 145 NaCl, 4 KCl, 2 Na-pyruvate, 5 HEPES, 5 glucose, 2 $CaCl_2$, and 1 $MgCl_2$ (pH adjusted to 7.4 with NaOH). Voltage traces were sampled at 20 kHz, A/D converted at 16 bits, and stored on a personal computer employing the software LCG (Linaro et al., 2014). The same hardware/software system was employed to synthesize a variety of current-clamp stimulation waveforms, employed for estimating passive (i.e., membrane capacitance and input resistance) and active neuronal properties (i.e., rheobase current, frequency-current curve, spike-frequency adaptation index) of single cells. Recordings were analyzed off-line, employing custom scripts written in MATLAB (The MathWorks, Natick, US) or Excel (Microsoft, USA). The minor differences in AP's trajectory features (Fig. 2H, S3G) reflect the impact of hypoxia or DMOG on cell excitability (not significant).

Network-level extracellular recordings were performed in Neurobasal medium, supplemented with 1x B27 and 0.5 mM glutamine (Life Technologies). Across five distinct dissociation procedures, sister and non-sister cultures were plated on 28 multi-electrode arrays (MEAs). Hypoxic incubation was made in 1% O_2, 5% CO_2, and 94% N_2 atmosphere. The DMOG treatment was performed by adding it to the MEAs' bath at 1 mM final concentration. The described experiments were made overnight between DIV 13-14 and 20-21. Lentiviral transduction was accomplished by incubating overnight the neurons with 10 MOI particles. The electric network activity was recorded on all MEAs at DIV 13,14,15, and from DIV 20 to 22 only for hypoxia experiments. Electrophysiological recordings were performed by means MEA1060BC amplifiers, (Multichannel Systems GmBH, Reutlingen, Germany) inside an electronic friendly incubator, maintaining 37°C, 5% CO2, and 100% R.H. This allowed us to monitor simultaneously, chronically, and non-invasively the neuronal electrical activity from up to 59 locations within the very same culture. MEA recordings were analyzed off-line by QSpikeTools (Mahmud et al., 2014). Briefly, the extracellular electric fields were monitored from up to 59 independent electrodes in each MEAs, sampled at 25 kHz / channel, 1200x amplified, bandpass-filtered (400-3000Hz), and digitally recorded for 60 min every day. Elementary spike-sorting, only based on spike-shape peak polarity, was performed. Epochs of spontaneous synchronized firing across the MEAs electrodes were identified over 1 ms bins and by employing a threshold equal to 10. Neurons excitability in all MEAs was probed by low frequency (0.2 Hz) electrical extracellular stimulation, employing a stimulus isolator (STG1002, Multichannel Systems, Germany) programmed and driven by a custom made MATLAB (The MathWorks, USA). Four electrodes were chosen after probing 10 random sites of all electrodes. Stimuli were characterized by a square biphasic waveform of 1 ms duration and 1.6 V amplitude.

SUPPLEMENTAL REFERENCES

Aragones, J., Jones, D.R., Martin, S., San Juan, M.A., Alfranca, A., Vidal, F., Vara, A., Merida, I., and Landazuri, M.O. (2001). Evidence for the involvement of diacylglycerol kinase in the activation of hypoxia-inducible transcription factor 1 by low oxygen tension. J Biol Chem *276*, 10548-10555.

Arranz, A.M., Delbroek, L., Van Kolen, K., Guimaraes, M.R., Mandemakers, W., Daneels, G., Matta, S., Calafate, S., Shaban, H., Baatsen, P.*, et al.* (2015). LRRK2 functions in synaptic vesicle endocytosis through a kinase-dependent mechanism. J Cell Sci *128*, 541-552.

Attardo, A., Calegari, F., Haubensak, W., Wilsch-Brauninger, M., and Huttner, W.B. (2008). Live imaging at the onset of cortical neurogenesis reveals differential appearance of the neuronal phenotype in apical versus basal progenitor progeny. PLoS One *3*, e2388.

Goedhart, J., von Stetten, D., Noirclerc-Savoye, M., Lelimousin, M., Joosen, L., Hink, M.A., van Weeren, L., Gadella, T.W., Jr., and Royant, A. (2012). Structure-guided evolution of cyan fluorescent proteins towards a quantum yield of 93%. Nat Commun *3*, 751.

Haase, V.H., Glickman, J.N., Socolovsky, M., and Jaenisch, R. (2001). Vascular tumors in livers with targeted inactivation of the von Hippel-Lindau tumor suppressor. Proceedings of the National Academy of Sciences of the United States of America *98*, 1583-1588.

Hotulainen, P., Llano, O., Smirnov, S., Tanhuanpaa, K., Faix, J., Rivera, C., and Lappalainen, P. (2009). Defining mechanisms of actin polymerization and depolymerization during dendritic spine morphogenesis. J Cell Biol *185*, 323-339.

Iliopoulos, O., Kibel, A., Gray, S., and Kaelin, W.G., Jr. (1995). Tumour suppression by the human von Hippel-Lindau gene product. Nat Med *1*, 822-826.

Kayser, M.S., Nolt, M.J., and Dalva, M.B. (2008). EphB receptors couple dendritic filopodia motility to synapse formation. Neuron *59*, 56-69.

Leite de Oliveira, R., Deschoemaeker, S., Henze, A.T., Debackere, K., Finisguerra, V., Takeda, Y., Roncal, C., Dettori, D., Tack, E., Jonsson, Y.*, et al.* (2012). Gene-targeting of Phd2 improves tumor response to chemotherapy and prevents side-toxicity. Cancer cell *22*, 263-277.

Linaro, D., Couto, J., and Giugliano, M. (2014). Command-line cellular electrophysiology for conventional and real-time closed-loop experiments. J Neurosci Methods *230*, 5-19.

Livet, J., Weissman, T.A., Kang, H., Draft, R.W., Lu, J., Bennis, R.A., Sanes, J.R., and Lichtman, J.W. (2007). Transgenic strategies for combinatorial expression of fluorescent proteins in the nervous system. Nature *450*, 56-62.

Mahmud, M., Pulizzi, R., Vasilaki, E., and Giugliano, M. (2014). QSpike tools: a generic framework for parallel batch preprocessing of extracellular neuronal signals recorded by substrate microelectrode arrays. Front Neuroinform *8*, 26.

Marom, S., and Shahaf, G. (2002). Development, learning and memory in large random networks of cortical neurons: lessons beyond anatomy. Q Rev Biophys *35*, 63-87.

Niwa, H., Yamamura, K., and Miyazaki, J. (1991). Efficient selection for high-expression transfectants with a novel eukaryotic vector. Gene *108*, 193-199.

O'Gorman, S., Fox, D.T., and Wahl, G.M. (1991). Recombinase-mediated gene activation and site-specific integration in mammalian cells. Science *251*, 1351-1355.

Ruiz de Almodovar, C., Fabre, P.J., Knevels, E., Coulon, C., Segura, I., Haddick, P.C., Aerts, L., Delattin, N., Strasser, G., Oh, W.J.*, et al.* (2011). VEGF mediates commissural axon chemoattraction through its receptor Flk1. Neuron *70*, 966-978.

Ryan, H.E., Poloni, M., McNulty, W., Elson, D., Gassmann, M., Arbeit, J.M., and Johnson, R.S. (2000). Hypoxia-inducible factor-1alpha is a positive factor in solid tumor growth. Cancer Res *60*, 4010-4015.

Shaner, N.C., Campbell, R.E., Steinbach, P.A., Giepmans, B.N., Palmer, A.E., and Tsien, R.Y. (2004). Improved monomeric red, orange and yellow fluorescent proteins derived from Discosoma sp. red fluorescent protein. Nat Biotechnol *22*, 1567-1572.

Sorra, K.E., and Harris, K.M. (2000). Overview on the structure, composition, function, development, and plasticity of hippocampal dendritic spines. Hippocampus *10*, 501-511.

Spiga, S., Acquas, E., Puddu, M.C., Mulas, G., Lintas, A., and Diana, M. (2011). Simultaneous Golgi-Cox and immunofluorescence using confocal microscopy. Brain Struct Funct *216*, 171-182.

Tronche, F., Kellendonk, C., Kretz, O., Gass, P., Anlag, K., Orban, P.C., Bock, R., Klein, R., and Schutz, G. (1999). Disruption of the glucocorticoid receptor gene in the nervous system results in reduced anxiety. Nature genetics *23*, 99-103.

Wilm, M., Shevchenko, A., Houthaeve, T., Breit, S., Schweigerer, L., Fotsis, T., and Mann, M. (1996). Femtomole sequencing of proteins from polyacrylamide gels by nano-electrospray mass spectrometry. Nature *379*, 466-469.

Woo, M.S., Ohta, Y., Rabinovitz, I., Stossel, T.P., and Blenis, J. (2004). Ribosomal S6 kinase (RSK) regulates phosphorylation of filamin A on an important regulatory site. Molecular and cellular biology *24*, 3025-3035.

Ziv, N.E., and Smith, S.J. (1996). Evidence for a role of dendritic filopodia in synaptogenesis and spine formation. Neuron *17*, 91-102.